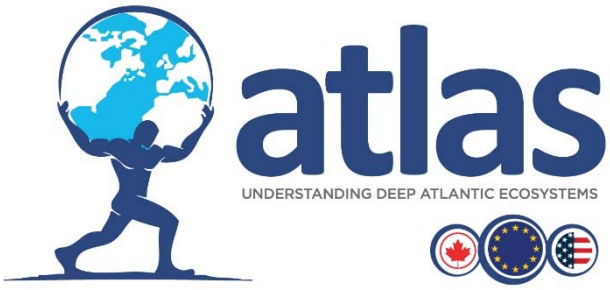

ATLAS Deliverable 2.4:

Water mass properties, hydrodynamic controls and mechanisms of organic matter supply in ATLAS case study areas

Project acronym:	ATLAS
Grant Agreement:	678760
Deliverable number:	2.4
Deliverable title:	Report of the in-situ hydrodynamics, abiotic variables, and suspended particles near the seafloor and sedimenting particles from bottom traps to identify organic matter transport pathways for different case study sites and a qualitative comparison with output from the high-resolution hydrodynamic models during periods of strong and weak AMOC.
Work Package:	2
Date of completion:	28-06-2019
Author:	Christian Mohn, Dick van Oevelen
Co-Authors (in alphabetical order):	Marina Carreiro-Silva, Carlos Domínguez Carrió, Gerard Duineveld, Alan Fox, Stefan Gary, Erica Head, Jørgen L.S. Hansen, Ellen Kenchington, Laura Korte, Furu Mienis, Telmo Morato, Eva Friis Møller, Maria Rakka, Lorenzo Rovelli, Kirstin Schulz, Karline Soetaert, George Wolff, Igor Yashayaev

This project has received funding from the European Union's Horizon 2020 research and innovation programme under grant agreement No 678760 (ATLAS). This output reflects only the author's view and the European Union cannot be held responsible for any use that may be made of the information contained therein.

Contents

1 Executive Summary

The EU-H2020 ATLAS project provides a multi-disciplinary framework for investigating and quantifying interactions and connections of sensitive deep-sea ecosystems. ATLAS aims to develop an improved understanding of deep-sea ecosystem functioning and ecosystem responses to changes in human use and ocean climate at different temporal and spatial scales reaching from the basin-wide North Atlantic to individual and diverse case study areas. The Atlantic Meridional Overturning Circulation (AMOC) and associated large-scale gyre systems play a pivotal role for energy and material transport in the North Atlantic and for regulating climate and environmental variability. ATLAS developed high-resolution ocean circulation models and collected in-situ data of near-bottom currents, water mass properties, suspended and sedimenting particles in the water column as well as near the seafloor in three environmentally contrasting case study areas (Davis Strait, southeast Rockall Bank, Condor Seamount). This unique combination of hydrodynamic models and in-situ observations provides new insights of feedbacks of large-scale ocean climate change on local ecosystem-scale dynamics and food supply mechanisms in ecologically sensitive areas. Benthic filter feeders live and thrive under special environmental conditions in which abiotic and biotic factors including temperature, bottom roughness, currents and food supply are equally important. In this report, we will present data from ATLAS in-situ observations (Rockall Bank, Condor Seamount, Davis Strait) and pre-ATLAS data (Condor Seamount) in combination with ATLAS model data to estimate patterns and physical drivers of food supply and their variability in space and time. The main objective is to describe local-scale and largely tidally dominated mechanisms of food supply to benthic organisms, feeding ecology and organic matter cycling in response to characteristic changes of the AMOC. While the Rockall Bank comprises the most complete data set of the three study sites, observations from Condor Seamount and Davis Strait are still being progressed.

2 State of the AMOC in ATLAS case study areas from analysis of VIKING20 data

Data are obtained from a 53-year VIKING20 model hindcast developed by GEOMAR in Kiel, Germany, in the EU-FP7 project THOR (2007-2013, grant no 212643, e.g. Böning et al 2016). The VIKING20 model is a nest of the polar and sub-polar North Atlantic embedded in the global ocean general circulation model ORCA025 (1/4° resolution). The VIKING20 model is eddy-resolving with a spatial resolution of 1/20° with prescribed atmosphere covering the North Atlantic in the latitudinal range 30 °N - 80 °N. The model output includes a large set of prognostic and diagnostic 2D and 3D variables, including temperature, salinity, sea surface height, mixed layer depth, 3D currents, and atmosphere and ocean fluxes. All model output parameters are made available as 5-day averages, i.e. 73 records per parameter and year. VIKING20 data were extracted for three ATLAS case study areas (Davis Strait, Rockall Bank, Condor Seamount) for the period 1958 – 2009 (see Figure 2.1 for an overview). These areas represent different eco-regions of the N-Atlantic. Davis Strait hosts rich *Geodia* spp. sponge grounds (Knudby et al. 2013), large cold-water coral carbonate mounds and *Lophelia pertusa* reefs can be found at southeast Rockall Bank in the depth range 800 to 1200 m (e.g. White et al. 2007, Duineveld et al. 2007). Benthic communities at the summit of Condor seamount are dominated by dense coral gardens formed by the octocorals *Viminella flagellum* and *Dentomuricea* c.f. *meteor* at depths between 185 and 287 m depth (Tempera et al. 2012).

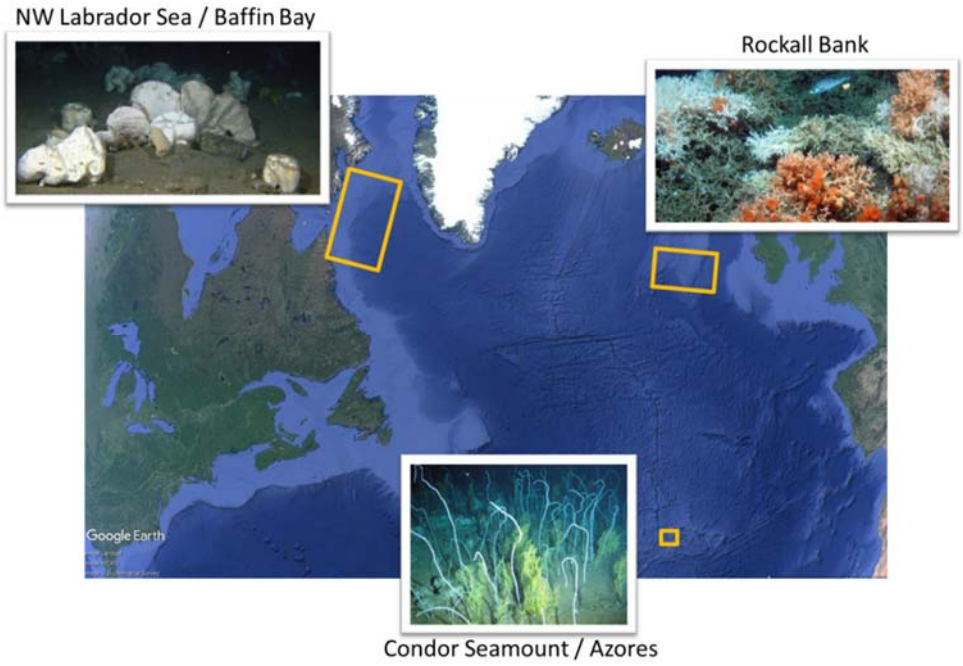

Figure 2.1: Overview about ATLAS case study areas for analysis of long-term changes of the basin-scale ocean climate and high-resolution modelling of hydrodynamics and organic matter cycling.

Our analysis compares time series of near-bottom and depth-averaged currents from the VIKING20 model with relevant ocean climate indices (Atlantic Meridional Overturning Circulation AMOC, Subpolar Gyre Index SPG) to identify periods of distinctive ocean climate states in the VIKING20 data in every case study area. These periods were used as reference periods to investigate basin-scale climate feedbacks in case study areas using a high-resolution hydrodynamic model.

Basin-scale physical processes in the upper ocean and deep water North Atlantic often follow multi-annual spatial and temporal patterns, which often are presented in ocean climate indices (for an overview see Johnson et al. 2019). In this report, we focus on one specific index, the AMOC. The AMOC represents the strength of the overturning circulation in the North Atlantic and is an indicator for the conversion of upper waters to dense intermediate and deep waters (Johnson et al. 2019 and references therein). South of 40 °N, the AMOC is characterized by periods of weak AMOC from the early 1960s to the late 1980s and strong AMOC since the late 1980s. The most pronounced end members appeared in two periods, 1978 – 1981 (weak AMOC) and 1992-1999 (strong AMOC) respectively (Figure 2.2). North of 40 °N, at mid and high latitudes, AMOC variability is more pronounced and occasionally out of phase with conditions in the subtropical and tropical Atlantic. However, the most intense weak and strong AMOC states were also predicted for the late 1970s and early 1990s (Figure 2.2).

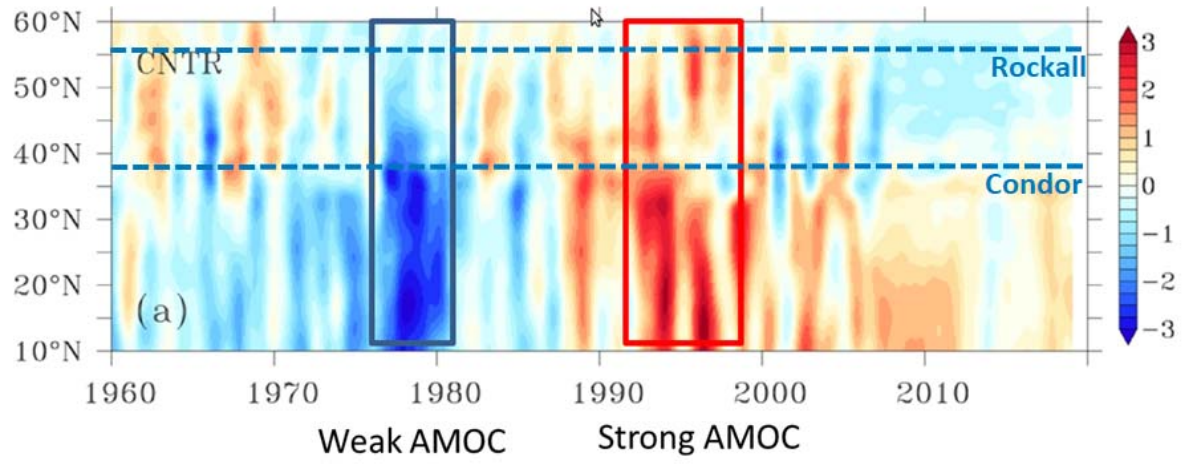

Figure 2.2: VIKING20 basin wide AMOC anomalies. This figure was reproduced from Böning et al (2016) from their supplementary information, Figure 4c. Examples for periods/years of low (weak) AMOC state: 1978-1981 across a range of subpolar/subtropical latitudes. Periods/years of high (strong) AMOC state: 1992-1999. Blue dashed lines indicate the latitude of Rockall Bank and Condor Seamount.

AMOC anomalies are closely linked to the dynamics of the North Atlantic gyre system. Figure 2.3 shows modelled and observed changes of the subpolar gyre (SPG) expressed as the SPG index

(Hatun et al. 2005). The SPG index indicates the strength and lateral extension of the subpolar gyre across the North Atlantic. Periods of a weak gyre index correspond to positive basin-wide salinity anomalies and a weak state of the AMOC, whereas periods of a strong subpolar gyre correspond to negative basin-wide salinity anomalies and a strong AMOC state (Figure 2.3 b).

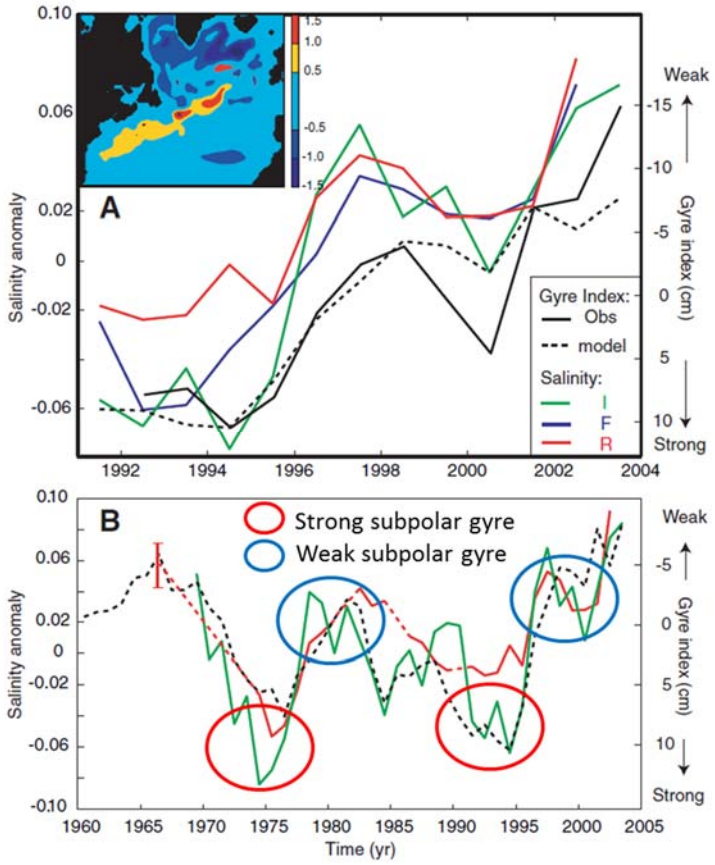

Figure 2.3: Subpolar Gyre Index (SPG), taken and modified from Hatun et al (2005). (A) Gyre index for the period 1992 – 2004 and (B) 1960 – 2005 in different regions of the North Atlantic (I = Irminger Current, F = Faroe Current, R = Rockall Bank).

Two model parameters from VIKING20 model data were analysed in ATLAS case study areas for comparison with basin-wide AMOC anomalies, near-bottom current magnitude and magnitude of depth-averaged currents. Each time series was averaged over the whole case study area prior to calculating anomalies for the reference period 1958-2009. Time series were filtered using 1-year and 5-year moving averages to remove seasonal variability and to retain the dominant inter-annual variability. Signals of strong and weak states of the AMOC and the SPG are well represented in time series of near-bottom and depth-averaged currents in the case study areas. The best agreement was found in the Davis Strait case study area (Figure 2.4). In the Rockall Bank and Condor Seamount regions (Figure 2.5, Figure 2.6), corresponding signals are less pronounced or occasionally out of phase with the basin wide AMOC. Based on this analysis, the years 1978 – 1980 (weak AMOC) and

1992 – 1994 (strong AMOC) were considered as the most characteristic and strongest changes of the basin-wide AMOC and chosen as boundary conditions for high resolution modelling of the Rockall Bank and Condor Seamount case study areas.

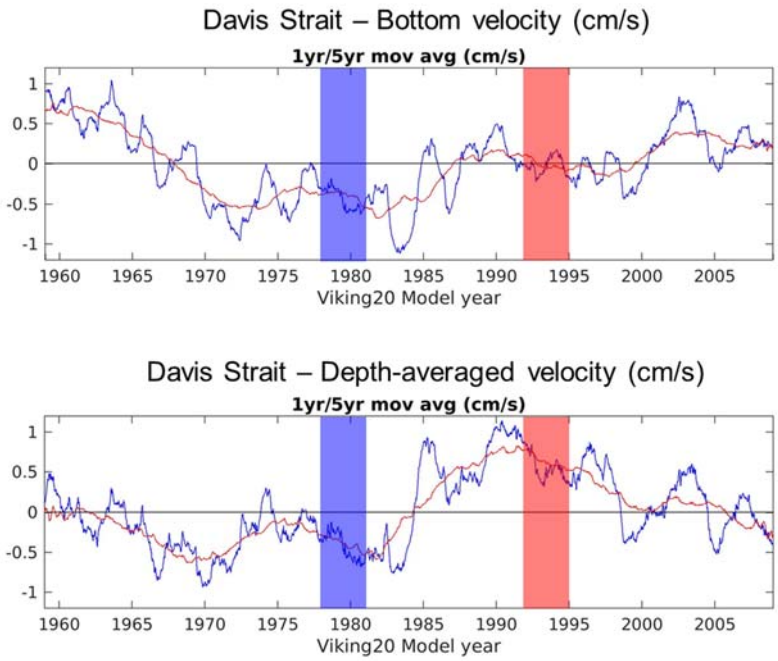

Figure 2.4: Bottom (top) and depth-averaged (bottom) current velocity anomalies from 1 (blue) and 5 (red) year running means (1958 – 2009) in the Davis Strait case study area. Red bars indicate periods of strong AMOC and a strong Subpolar Gyre Index. Blue bars indicate periods of weak AMOC and weak Subpolar Gyre index.

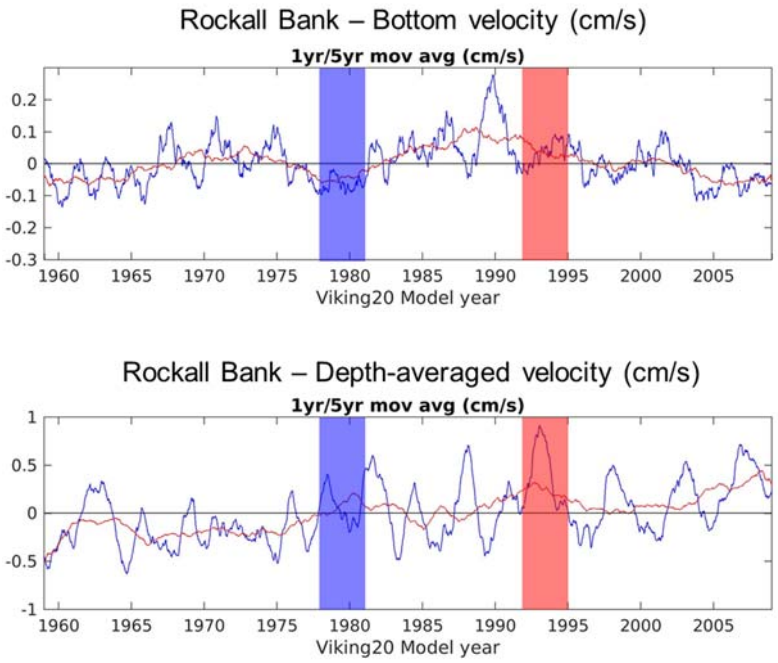

Figure 2.5: Bottom (top) and depth-averaged (bottom) current velocity anomalies from 1 (blue) and 5 (red) year running means (1958 – 2009) in the Rockall Bank case study area. Red bars indicate periods of strong AMOC and a strong Subpolar Gyre Index. Blue bars indicate periods of weak AMOC and weak Subpolar Gyre index.

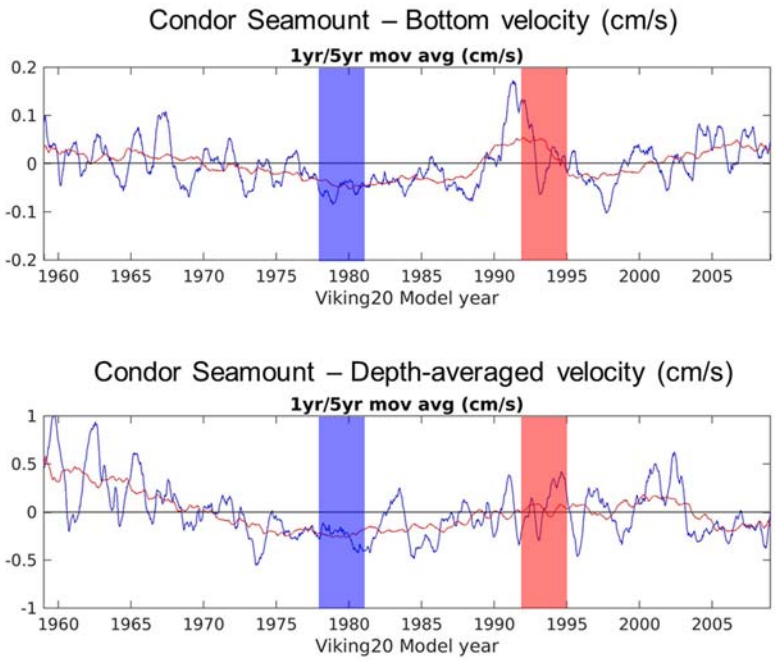

Figure 2.6: Bottom (top) and depth-averaged (bottom) current velocity anomalies from 1 (blue) and 5 (red) year running means (1958 – 2009) in the Condor Seamount case study area. Red bars indicate periods of strong AMOC and a strong Subpolar Gyre Index. Blue bars indicate periods of weak AMOC and weak Subpolar Gyre index.

3 High-resolution hydrodynamic model in two case study areas

The hydrodynamic model ROMS-Agrif (Regional Ocean Model System and adaptive grid refinement package, Shchepetkin and McWilliams, 2005) was used to assess local-scale feedback in two different case study areas (Rockall Bank, Condor Seamount) in response to characteristic changes of the AMOC in the past century. These changes are introduced as lateral boundary conditions derived from the 1/20° resolution VIKING20 North Atlantic model. The main objective was to investigate the importance of local-scale physical controls of food supply, feeding ecology and organic matter cycling (internal tides, bottom boundary layer dynamics) in comparison with patterns and variability introduced by large-scale ocean climate shifts. The main model results are published in Deliverable 2.5.

The setup of ROMS-Agrif in each case study area includes the following key features:

- Spatial resolution of nested computational grid (see Figure 3.1): 750 m (parent grid, providing boundary conditions to the embedded grid), 250 m (embedded grid), 32 terrain-following vertical levels in each grid.
- Boundary conditions: Lateral boundary conditions from the VIKING20 model data (T, S, currents, SSH) every five days, tidal forcing from the OSU inverse tidal model (Egbert and Erofeeva 2002), air-sea fluxes from the COADS climatology, bathymetry from the GEBCO 30 arc seconds dataset for parent grids, high-resolution multi-beam bathymetry for inner grids from local and regional seabed surveys (INSS, IMAR).
- Simulation period: 3 years within each characteristic AMOC endmember state (weak AMOC: 1978-1980, strong AMOC: 1992-1994).
- Model output: 2D sea surface height, 3D fields of water mass properties (T, S) and 3D currents (horizontal and vertical velocities).

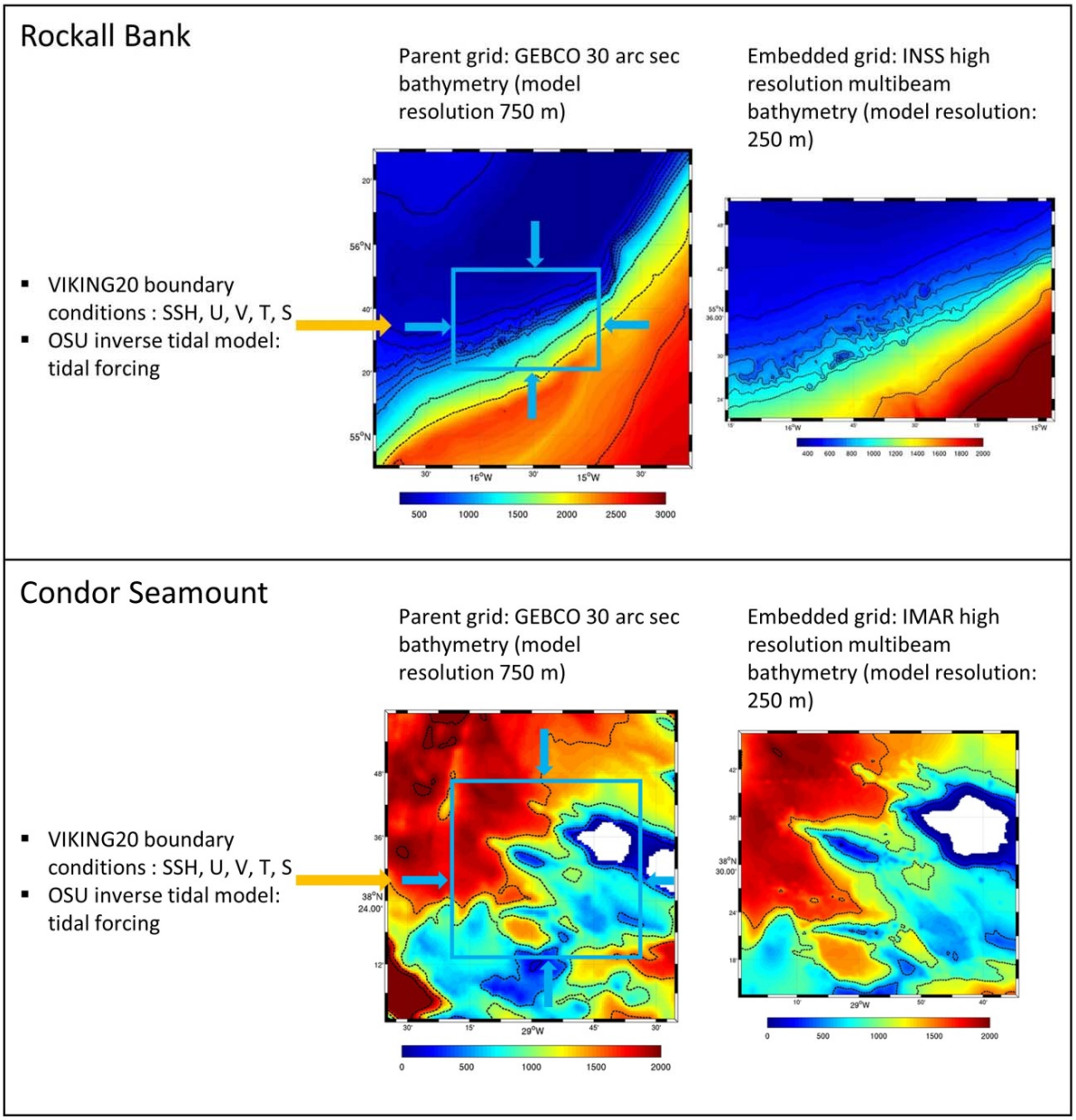

Figure 3.1: Model setup of high-resolution Roms-Agrif hydrodynamic model in case study areas Rockall Bank (top) and Condor Seamount (bottom). Lateral forcing at boundaries of the parent grid was obtained from VIKING20 model data (SSH, U, V, T, S) and the OSU inverse tidal model (tidal currents). The embedded, high-resolution grid received forcing data from the parent grid solutions. Coloured contours indicate water depth.

4 Case study areas

4.1 Rockall Bank

4.1.1 Site description

The Rockall Trough denotes the basin east of the European continental shelf, bounded by the Rockall Bank in the West and by the Wyville Thomson Ridge (WTR) in the North (Figure 4.1 A). The mean depth of the basin gradually increases from approximately 1000 m in the northern part to more than 3000 m at the open southern end. In the northern part, two seamounts with a depth of approximately 500 m interrupt the basin.

The trough itself forms an exchange pathway between water from the Eastern North Atlantic and the Nordic Seas. In the south, ENAW enters in the upper layers and is transported north-eastwards with the North Atlantic Current (NAC). Below, at a depth of around 700 m, the Shelf Edge Current transports North Atlantic Water (NAW; characterized by a higher salinity compared to ENAW) northwards along the eastern slope of the trough. At depths between 1600-1900 m, Labrador Sea Water (LSW) enters the basin and recirculates anticyclonic in the southern part of the basin, as the circulation is bounded by the shallow topography in the North. The same applies for the deepest water mass entering in the South, the Antarctic Bottom Water (AABW).

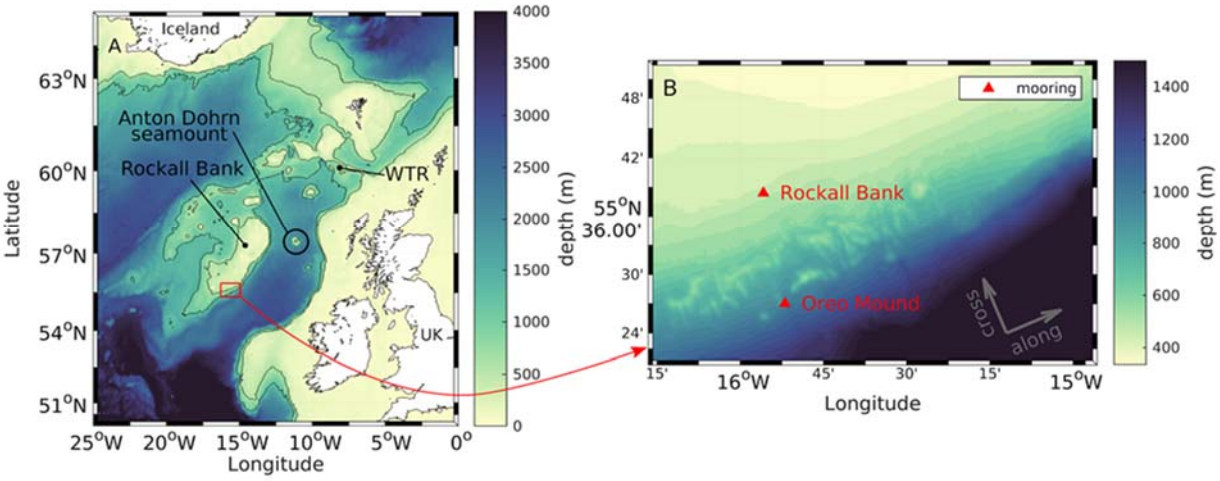

Figure 4.1: Left: Bathymetric map of the Rockall Trough, based on ETOPO-1 data, with the Rockall Bank and the Wyville Thomson Ridge (WTR) indicated. Black lines denote the 600 m and 1200 m isobaths. Right: Enlargement of the study area with positions of the moorings (red triangles) indicated. The orientation of the rotated coordinate system (matching the along- and cross-slope direction) is indicated in grey.

In the North, the warm ENAW and NAW are transported over the WTR into the Faroe-Shetland channel. The complex topography around the WTR results in the interaction of numerous water

masses in that region. The only water mass entering the Rockall Trough in the North is the Wyville Thomson Ridge Overflow Water (WTOW), which consists to a large part of Norwegian Sea Deep Water (NSDW). It passes the Anton Dohrn seamount on the western side and propagates as a slope current along the eastern flank of the Rockall Bank towards the south. In the western Rockall Trough, WTOW is found at depths of 600-1200 m and can be traced as far south as 55°N in the Rockall Trough (Johnson et al., 2010).

The Logachev mound province is located on the SE slope of the Rockall Bank (Figure 4.1 B). In this area, several carbonate mounds are present in a 90 km x 60 km area between 500- and 1000-meters water depth (Mienis et al. 2006). On these mounds, thriving coral reefs are found consisting of framework building *Lophelia pertusa* and *Madrepora oculata* with associated macrofauna such as polychaetes (e.g. *Eunice norvegica*), sponges (e.g. *Hexadella dedritifera*), and crinoids (Van Weering et al. 2003; Van Soest and Lavaleye 2005). Ambient bottom water temperatures on the coral mounds are between 7-9 °C and the area is characterised by the presence of hydrodynamical features such as internal tidal waves, hydraulic jumps and high bottom current speeds (Mohn et al. 2014, Van Haren et al. 2014, Cyr et al. 2016).

The largest carbonate mound in the region is Haas mound which resides at depths range of 900-m to 600-m. Oreo mound is a smaller carbonate mound SW of the Haas mound with the summit at 750-m water depth. The off-mound site is located further on the bank at a depth of 500 m (Figure 4.1 B). Previous work on the Logachev mound province, observed a patchy distribution of living corals alternating with bare sediments and coral rubble on the summit of the Haas mound, and a dense thriving cold-water coral reef on the southern flank of the Haas mound and the Oreo mound (Van Bleijswijk et al. 2015).

4.1.2 Overview of data, instrumentation and quality control

Cruises and instrumentation

The data presented on Rockall bank site were obtained during two cruises with the *RV* Pelagia. During the first cruise (64PE420, April 24 to May 12, 2017), two long term moorings were deployed at the slope of the Rockall Bank and on the Oreo mound, respectively. On May 8, 2017, a transect of CTD casts, starting from above the Oreo mound up the bank was performed. The mooring positions are indicated in Figure 4.1. During the second cruise (64PE436, April 29 to May 10, 2018), 24-hour long stationary CTD measurements were performed in the vicinity of each long-term mooring, before the moorings were recovered.

On both cruises, a CTD (SBE9/11+ from Sea-Bird Scientific, USA) was mounted on a steel frame, in the centre of a 24 Niskin bottle rosette, to measure profiles of temperature and salinity. The CTD was equipped with additional sensors for oxygen (SBE43), turbidity and chlorophyll (Wetlabs ECO-FLNTU). Data were collected at a frequency of 24 Hz and subsequently averaged to a vertical resolution of 1 dbar, using the Seasave software produced by SBE.

The Rockall bank mooring was deployed on May 2, 2017, at 09:00 UTC and recovered on May 5, 2018, at 13:45 UTC. Directly after deploying the mooring, its exact position of 55°38.44818' N, 15°55.839' W (507 m water depth) was determined by a triangulation of the release response signal. The mooring consisted of an anchor and two acoustic releasers at the bottom. On the mooring line, 23 m above the ground, a downward looking 2 MHz ADCP (Aquadopp from Nortek AS) and a fluorescence and turbidity sensor (Wetlabs FLNTU) was installed. The Aquadopp was programmed to record and internally average three measurements within 60 seconds every 30 minutes. The bin size was set to 0.5 m, with a total number of 20 bins and a blanking distance of 0.5 m. The FLNTU was programmed to record in intervals of 10 minutes. At 41 m above ground, an upward looking long-range 75 kHz ADCP (RDI Workhorse) was installed on a buoyancy unit. An average of 12 pings was recorded and stored every 20 minutes, the profiles included 74 bins of 8 m, with a blanking distance of 7 m. Data from both ADCPs were internally converted to ENU (East-North-Up) coordinates.

The mooring at the Oreo mound was deployed on May 9, 2017, at 11:00 UTC and recovered on May 5, 2018, 09:00 UTC. The exact position, again determined with a triangulation, was 55°27.048' N, 15°51.96798' W, at a water depth of 781 m. The lowermost part of the mooring was configured similarly to the one deployed at Rockall Bank. At 23 m above ground, a downward looking 2 MHz ADCP (Aquadopp from Nortek AS) and a Wetlabs FLNTU recorded in the same configuration as the respective instruments deployed at Rockall Bank. Due to a programming mistake, the Aquadopp did not record data before October 5, 2017. An upward looking 75 kHz ADCP (RDI Workhorse) was installed at a height of 41 m above the ground, profiling the water column in 99 bins of 4 m each, with a blanking distance of 12 m. Every 20 minutes, 20 pings were internally averaged and converted to ENU coordinates. An additional FLNTU, also recording in intervals of 10 minutes, was installed further up in the water column, at 425 m above the ground.

At both mooring lines, sediment traps were attached close to the bottom to collect the sinking particle fluxes. The cylindro-conical sediment traps (PPS 4/3) had a collecting area of 0.05 m^2 and a rotating carousel holding 12 sediment trap bottles. Sinking particles were collected in a time interval

of 23 to 30 days in each bottle. Total mass of particle fluxes was determined and the isotopic composition of nitrogen and organic carbon was analysed.

Inorganic nutrient and dissolved organic carbon data

Seven times during the 24-hour CTD station, i.e. at a roughly 4-hourly interval, the upcast of a CTD deployment was used to collect discrete water samples throughout the water column. A 12-L Niskin bottle, mounted on a Rosette sampler, was closed at 5-10 m above the bottom (judged from altimeter data), 50 mab, mid-water, within the deep chlorophyll maximum (typically around 50 mbs) and 5 mbs. Four times, i.e. a roughly 8-hour interval, the Niskin bottles were also sampled for pH, dissolved inorganic carbon (DIC) and total alkalinity and these samples were taken directly from the Niskin bottle after retrieval. For DIC, a 10-mL headspace vial was rinsed, filled completely, sealed with a crimp cap and transferred to a climate room, where the sample was poisoned through the septum with 10 µL saturated mercuric chloride ($HgCl_2$) for later analysis in the laboratory at NIOZ (Yerseke, The Netherlands). For alkalinity, a 50-mL Falcon tube was rinsed, filled, closed with a screw cap and transferred to a climate room, where the sample was poisoned with 50 µL saturated $HgCl_2$ for later analysis in the laboratory at NIOZ (Yerseke, The Netherlands). After taking these samples, the water from the Niskin bottles was emptied in 10 L carboys and transferred to the climate room for further processing. Nutrient samples were taken in the climate room with a 10 mL syringe equipped with a disposable 0.45 µm filter into 5-mL pony vials and subsequently frozen at -20^{o}C.

Data Quality and post-processing

The long-range ADCPs worked well most of the time. Profiles with a depth-averaged absolute error velocity greater than 0.06 m s^{-1} were found to result in (partly) unusable data and were consequently discarded. The fraction of discarded profiles for every week is displayed in Figure 4.2.

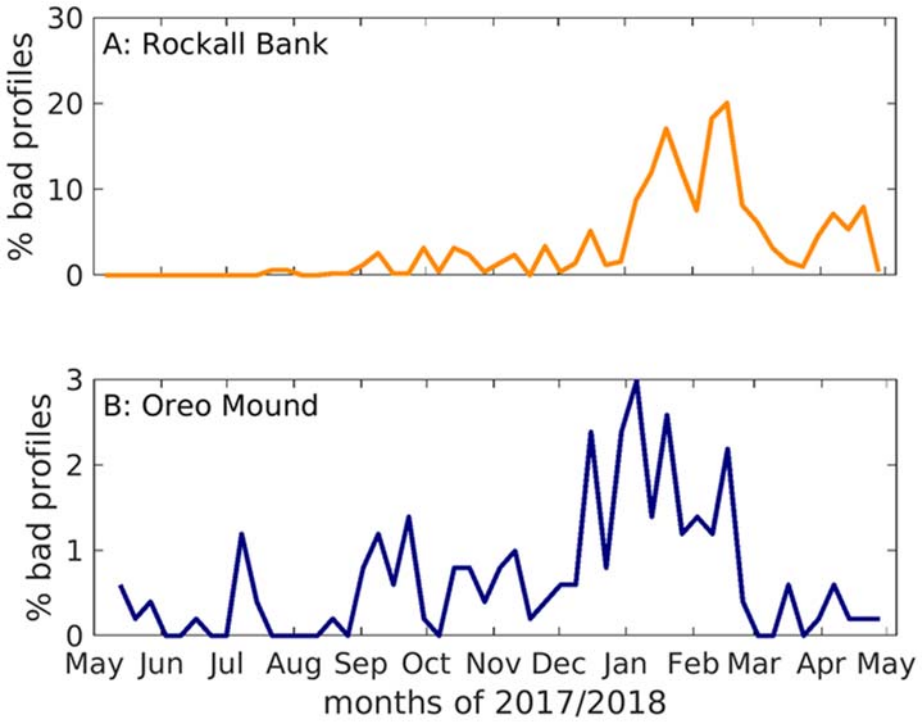

Figure 4.2. Weekly fraction of discarded profiles for the LR ADCP deployed at (a) Rockall Bank and (b) Oreo Mound.

While over 97% of the profiles recorded at Oreo Mound were usable throughout the year, up to 23% of the data obtained during the winter months at Rockall Bank had to be discarded. This resulted in gaps in the data of maximal 13 hours and 5 hours at Rockall Bank and Oreo Mound, respectively. Possible reasons for unusable profiles are, amongst others, a low concentration of backscatters in the water column (the acoustic signal from low-frequency ADCPs is typically reflected on particles of the size of zooplankton), blocking of the acoustic signal by e.g. the mooring rope, or an excessive tilt of the instrument. An estimation of the vertical current velocities from the long-range ADCPs proved to be impossible, as the instruments precision is insufficient to reliably detect these comparably small velocities.

For both of the deployed Aquadopps, which were situated close to the sea floor, the backscatter intensity of their acoustic signals was most of the time insufficient to obtain reliable data at distances further than 2 to 3 m away from the transducer head. This was presumably caused by a low concentration of suitable particles (which are in the diameter range of around 10--500 □m) in the near bottom layer. According to the documentation of the manufacturer, the amplitude threshold for reliable data is 6 counts above noise level, which was found to be 24 (20) for the Aquadopp deployed at Rockall Bank (Oreo Mound). Consequently, measurements with an amplitude

lower than 30 (26) were considered to be unreliable. In Figure 4.3, the fraction of measurements with insufficient amplitude per bin are displayed. As this fraction is rapidly increasing with distance from the transducer head, only data from the first 5 (4) bins from the Aquadopp deployed at Rockall Bank (Oreo Mound) were used in the following analysis.

Data from all ADCPs was rotated by 23 degrees to match the coordinate system indicated in Figure 4.1 B.

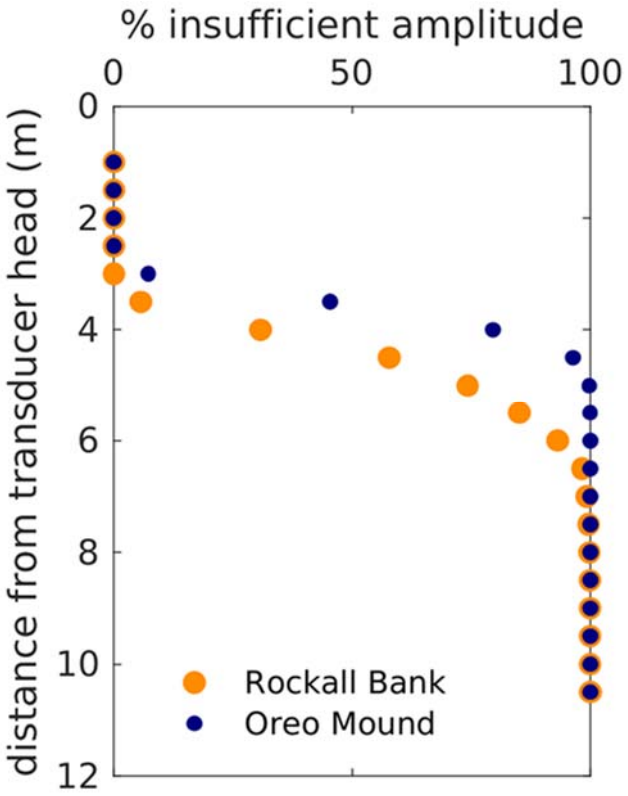

Figure 4.3. The fraction of samples with insufficient backscatter amplitude for each measuring bin of the Aquadopp deployed at Rockall Bank (orange dots) and at Oreo Mound (blue dots).

Turbidity and fluorescence data from the three moored FLNTUs were de-spiked and quality controlled. The turbidity signal of the sensor moored at Rockall Bank showed a sudden increase up to its maximum range after February 11, 2018. This might be a result of biofouling, and turbidity data after that event was discarded. The corresponding fluorescence signal exhibited a contemporaneous increase but remained below its maximum value. This data was therefore not discarded but should be treated with care as the sensor might be partly blocked as well. Fluorescence data from the upper sensor at Oreo Mound was corrected for a baseline drift (of +2 counts) that occurred on September 5, 2017, 05:00 UTC.

In addition, the three FLNTU sensors were intercalibrated by lowering them simultaneously with the CTD. Linear transfer functions were obtained for the fluorescence and turbidity data using the Theil-Sen method, which is a non-parametric method for robustly fit a line to sample points in the plane (simple linear regression) by choosing the median of the slopes of all lines through pairs of points. The deep Oreo Mound FLNTU was used as reference sensor. The transfer functions are summarized in Table 4.1. The sensitivity of the turbidity sensor from the FLNTU deployed at the upper position on the Oreo Mound mooring was insufficient for the encountered turbidity range. The data was therefore omitted.

Table 4.1. Coefficients of the linear transfer functions with respect to data from the deep Oreo Mound FLNTU.

Sensor	Slope	Intercept
fluorescence Rockall Bank	0.9340	- 14.8
fluorescence Oreo Mound shallow	7.8178	- 40.8
turbidity Rockall Bank	0.9092	- 39.1

4.1.3 Results

Water column structure

CTD transect (2017)

Data along the transect were obtained at May 8, 2017, starting at 08:20 UTC above Oreo Mound. The following CTD casts towards Rockall Bank were performed equidistantly spaced every 3 km, with the last station 95 being recorded at 20:25 UTC. When interpreting the results, it must be born in mind that the respective CTD casts were taken over half a diurnal cycle, and therefore during different tidal phases.

The water temperature across the transect is decreasing with depth, from approximately 11°C at the surface to 9°C near the bottom at the shallower parts of the transect, and 8°C in the deepest parts (Figure 4.4). Changes in salinity are rather small (Figure 4.4 B) and judging from temperature and

salinity variations, no distinctly different water masses are visible along the transect. Oxygen concentration (Figure 4.4 C) decreases with depth, with values ranging between up to 280 µmol kg^{-1} near the surface to 170-210 µmol kg^{-1} below 500 m depth. High turbidity values are confined to the surface layer throughout the transect and the near bottom layer in the shallower parts (0-25 km) (Figure 4.4 D). Fluorescence is only enhanced in the near surface layer (Figure 4.4 E).

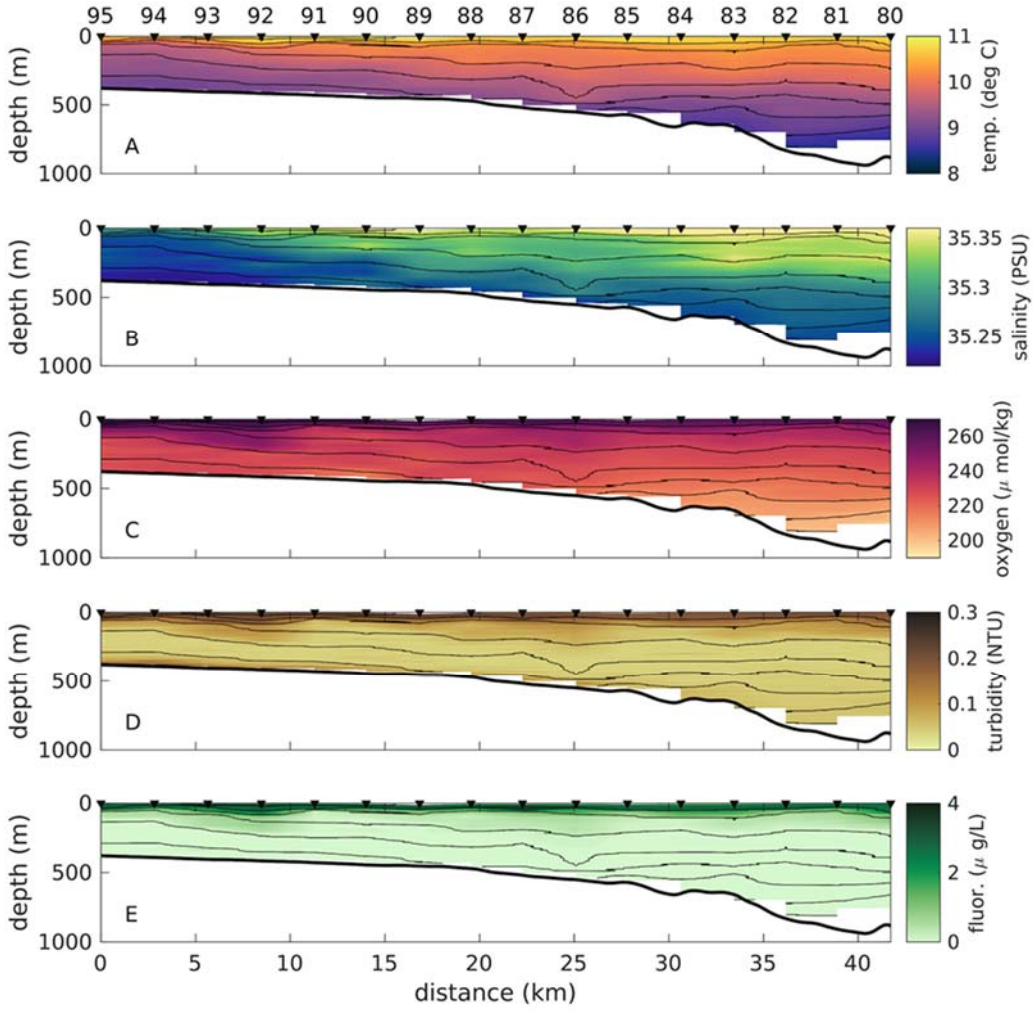

Figure 4.4: A) temperature, B) practical salinity, C) oxygen concentration, D) turbidity and E) fluorescence along a transect from Oreo mound onto the shallower Rockall Bank, essentially between both long-term mooring stations. The positions of the CTD casts are indicated with black triangles, the numbers on top refer to the station numbers. Black lines denote isopycnals with a spacing of 0.04 kg m^{-3}.

24-hour CTD yoyo's near mooring station Rockall Bank

Data from the 24-hour CTD station near the mooring at Rockall Bank, and the corresponding current velocity data from the moored long-range ADCP show a clear diurnal signal and are rather homogeneous in the vertical (Figure 4.5). The water column exhibits the classical profile consisting of a surface mixed layer (SML), a weakly stratified interior region and a bottom mixed layer (BML). The

SML extends to a depth of 50 to 100 m and is characterized by a relatively high oxygen concentration of approximately 260 µmol kg^{-1}. In the interior region below, oxygen concentrations are approximately 240 µmol kg^{-1}. A strong decrease in oxygen concentrations is visible in the BML (the lowermost 30 to 100 m of the water column), especially during the first half of the 24-hour cycle. Concentrations are as low as 210 µmol kg^{-1} and coincide with comparably low salinity values. Enhanced turbidity and fluorescence values are confined to the SML, and no turbid bottom boundary layer (BBL) is present. Occasional patches of turbidity are visible in the interior region, but their distribution is not coherent and unrelated to e.g. density interfaces.

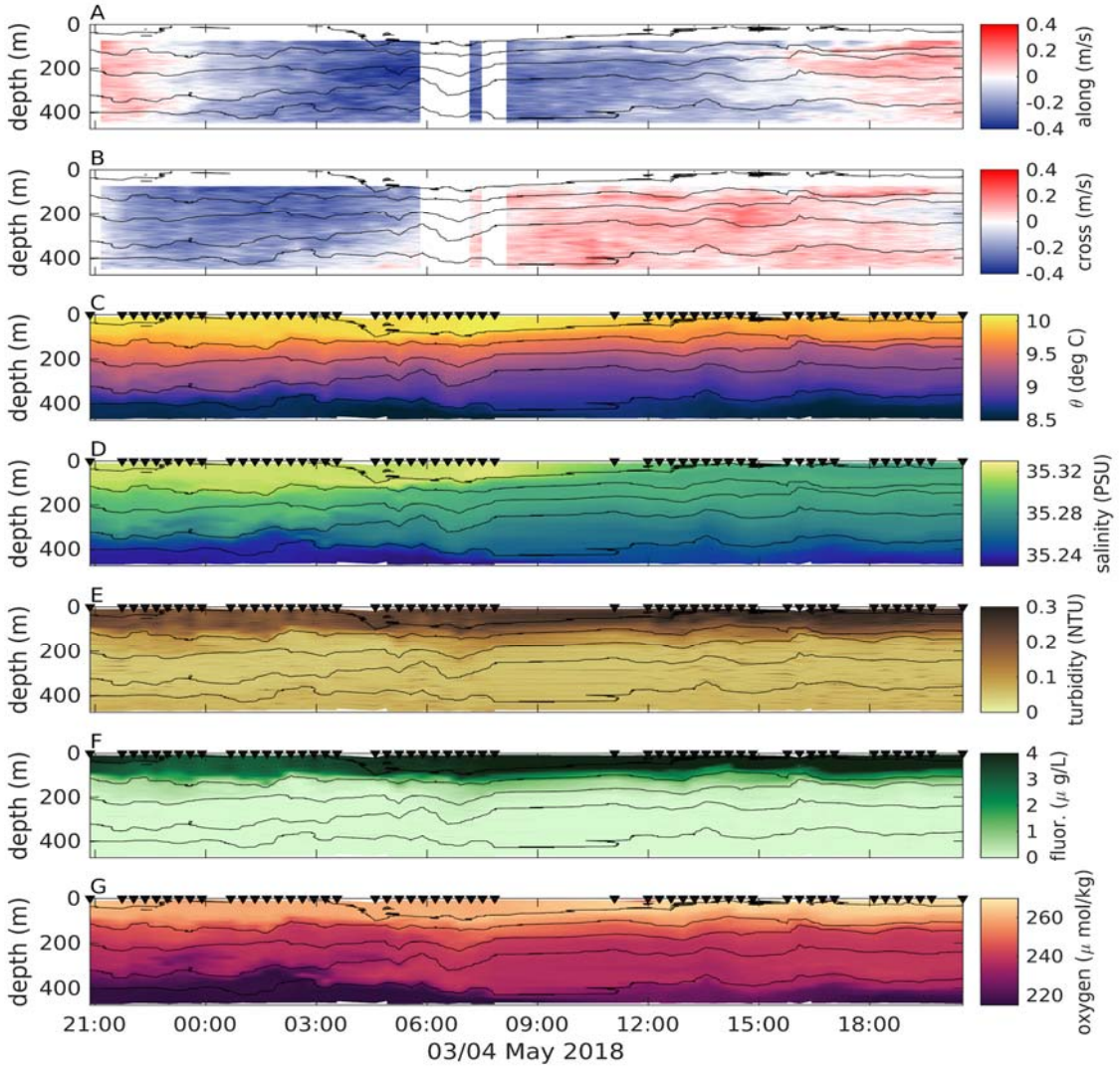

Figure 4.5. A) Along- and B) cross-slope current, obtained with the long range ADCP, C) potential temperature, D) practical salinity, E) turbidity, F) fluorescence and G) oxygen concentration, obtained with CTD casts above Rockall Bank. The individual casts are marked with black triangles, black lines denote isopycnals with a spacing of 0.04 kg m^{-3}.

24-hour CTD yoyo's near mooring station Oreo Mound

The vertical structure of the tidal current and the water column is substantially different at Oreo Mound compared to Rockall Bank (Figure 4.6 A, B). Above Oreo Mound, the currents are strongly sheared, intermittent and do not exhibit a clear tidal signal (Figure 4.6 A, B). The isopycnal displacement is much stronger than at Rockall Bank. The oxygenated surface layer has a comparable extent as at Rockall Bank, and enhanced values of turbidity and fluorescence are confined to this upper layer while they decrease rapidly below. The stratification in the interior region further increases below a depth of 400 to 600 m. In most of the profiles, a sharp increase in density with a coinciding decrease in oxygen concentration occurs at a depth between 600 and 750 m. This interface corresponds to a potential density of 27.4 kg m^{-3} (lowermost isoline in Figure 4.6 A-G) and an oxygen concentration of 222 µmol kg^{-1} (blue line in Figure 4.6 G). The relative height of the density interface seems to be correlated with the near-bottom cross-slope current: during the first 6 hours of the measurements, the near-bottom current is directed down-slope (Figure 4.6 B) and the observed layer thickness is decreasing, while during the last 6 hours, the cross-slope current is directed up-slope and the layer thickness is increasing. This demonstrates that a distinctly different water mass is present at the measurement location, and its relative position in the water column is modulated by the (diurnal) currents.

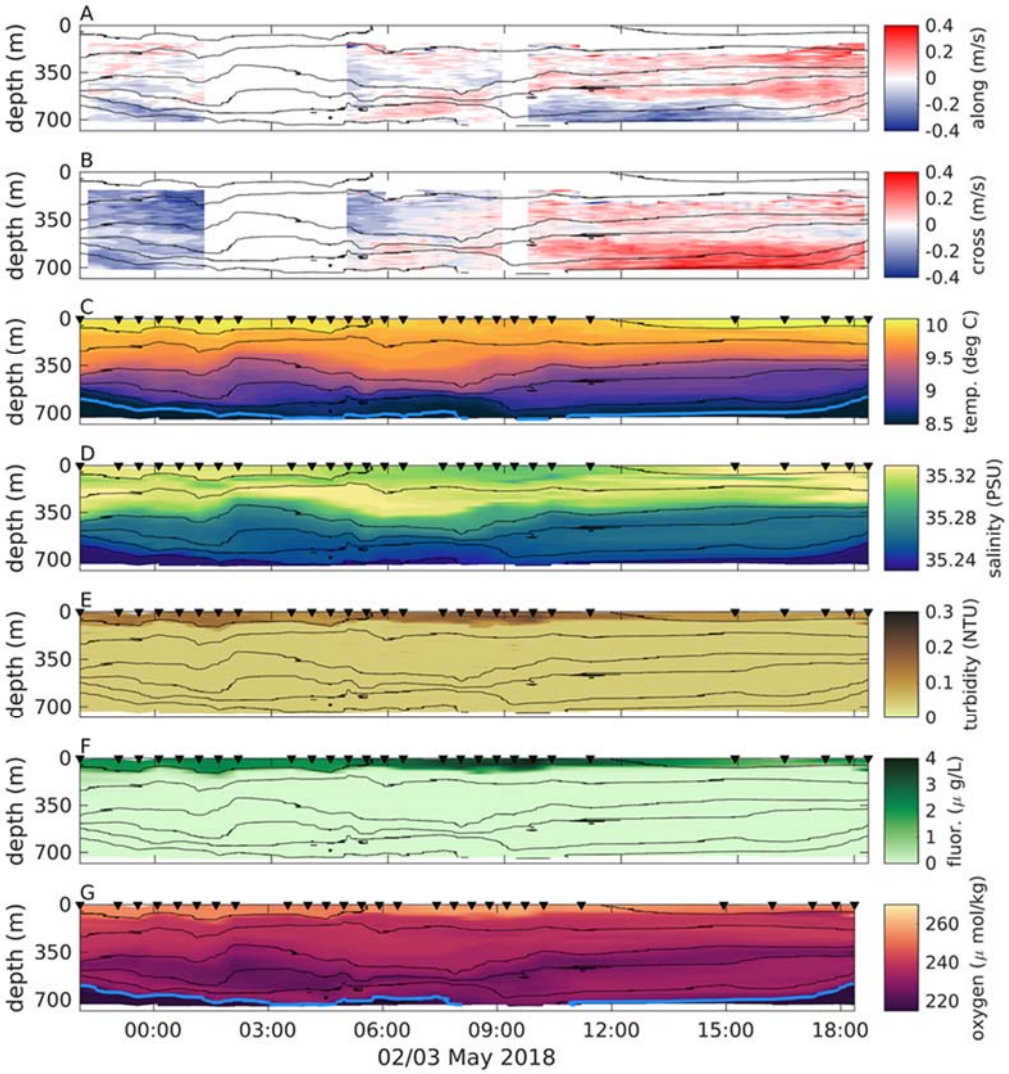

Figure 4.6: A) Along- and B) cross-slope current, obtained with the long range ADCP, C) potential temperature (with the 8.4°C isoline indicated in blue), D) practical salinity, E) turbidity, F) fluorescence and G) oxygen concentration (with the 222 µmol kg^{-1} isoline indicated in blue) obtained with CTD casts above Oreo mound. The individual casts are marked with black triangles, black lines denote isopycnals with a spacing of 0.04 kg m^{-3}.

Data from the CTD casts performed at Oreo Mound are displayed in a T-S diagram in Figure 4.7 B. As mentioned in the Rockall Bank site section (see above), the surface waters in the western Rockall Trough are dominated by ENAW (solid line in Figure 4.7). The observed temperature of the surface waters was approximately 1°C warmer than classical ENAW, which might be a result of the comparably warm air temperature during the sampling (May) or the mixing of ENAW with a different, warmer water mass. The deeper water (which corresponds to the denser, oxygen poor water mass described in the context of Figure 4.6) is found to be on a mixing line parallel to that characteristic for WTOW, which was observed at a depth below 600 m in the western Rockall Trough

north of 55°N (Johnson et al. 2010). This water mass is absent at the shallower Rockall Bank station (Figure 4.7 A).

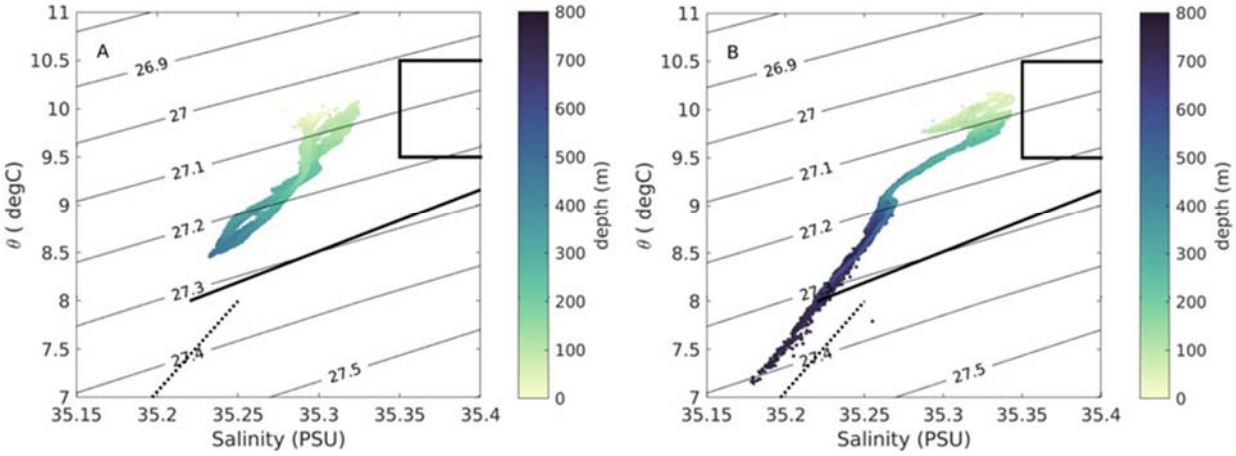

Figure 4.7: Salinity vs. potential temperature of data from the 24-hour stations (May 2018) at (A) Rockall Bank and (B) Oreo Mound. Black lines denote isopycnals, colours refer to water depth of the respective measurements. The dashed line indicates the mixing line of Wyville Thompson Ridge Overflow Water (WTOW), the solid line the mixing line for Eastern North Atlantic Water (ENAW), the rectangle denotes the range of North Atlantic Water (NAW).

To further investigate the vertical water column structure and the distinct chemical characteristics of the respective water masses, sampled nutrient data from the 24hour CTD station at Oreo Mound are presented (Figure 4.8).

Nitrite values are elevated in the surface layer but are close to the detection level (Figure 4.8 A). Nitrate, phosphate and silicate concentrations are relatively low in the near surface layer, but elevated in the dense water mass, presumably WTOW, near the bottom, as compared to the mid-depth water mass (Figure 4.8 B, E). The observed nutrient concentrations in this water mass during our study (nitrate: 13 to 18 µmol L^{-1}, phosphate: 0.9 to 1.2 µmol L^{-1}, and silicate: 6 to 10 µmol L^{-1}) compare favourably with the only knowledge available (that of the author), literature values for nitrate (17.4 to 17.9 µmol L^{-1}), phosphate (0.99 to 1.12 µmol L^{-1}) and silicate (9.8 to 10.7 µmol L^{-1}) concentration in the WTOW from 2009 and 2010 (McGrath et al. 2012). Hence, the elevated nutrient concentrations, when compared to the overlying water, are another indication that the water mass observed in this study is WTOW. The observed DIC concentrations are, although less pronounced, also elevated in the WTOW. Together with the observed high nutrient and low oxygen concentrations, this indicates that the WTOW is comparably 'old', i.e. it has not been in contact with the atmosphere for a long time.

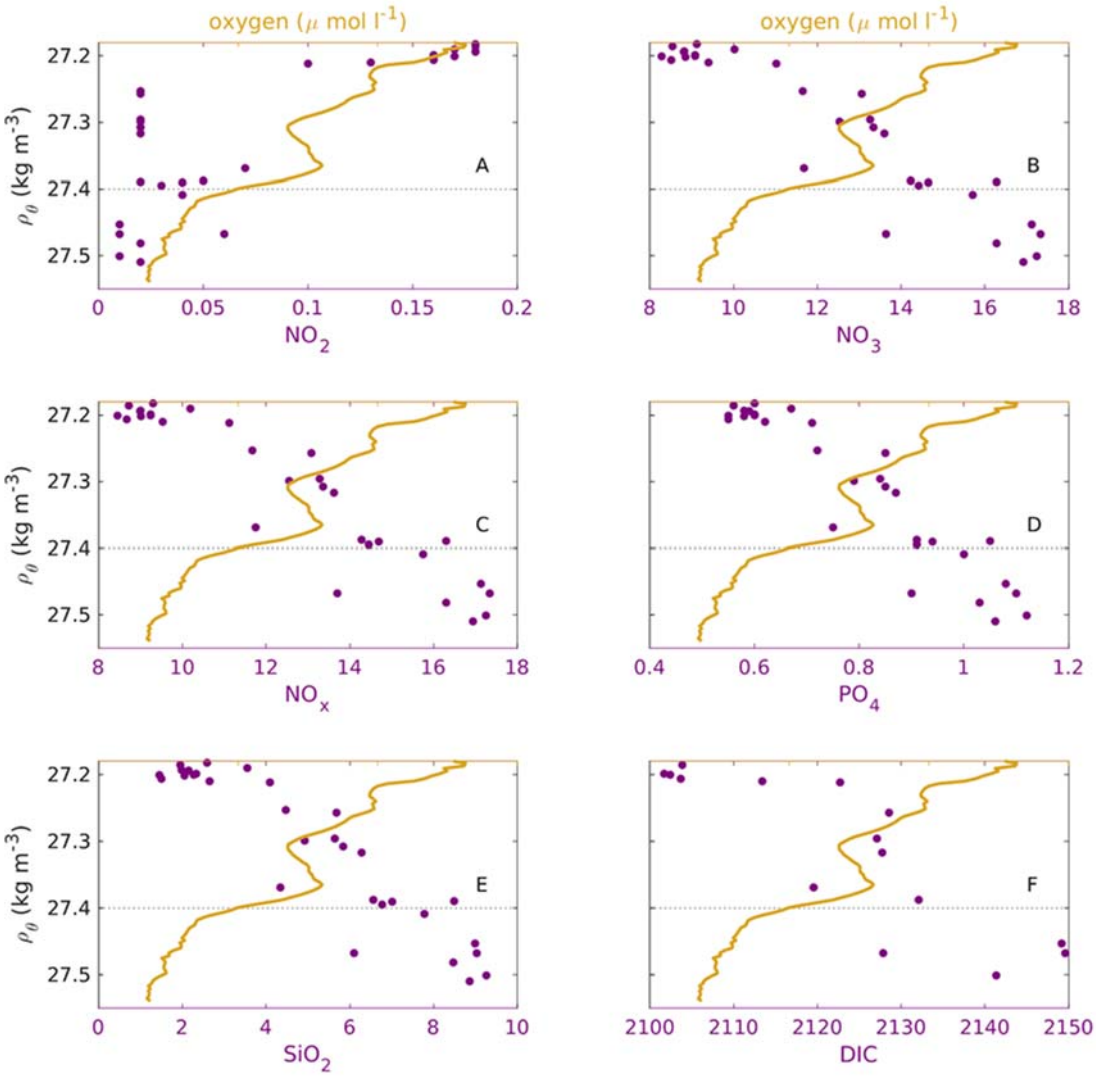

Figure 4.8. Vertical distribution of the observed A) nitrite, B) nitrate, C) total nitrogen, D) phosphate, E) silicate and F) dissolved inorganic carbon (DIC). All nutrients are in µmol L^{-1}. The vertical axis denotes potential density, instead of depth, to ease the distinction of the different water masses. The average oxygen profile is displayed in yellow for a better orientation; the horizontal dashed line indicates the approximate extent of the WTOW.

Long-term mooring data

Current velocity

The results presented in sections above give a first impression of the water column structure and the current regime in the vicinity of Oreo Mound, but comprise only one diurnal tidal cycle and may not be representative for the prevailing conditions. The data from the long-term moorings presented below, provide an insight on the annual mean conditions, as well as seasonal and smaller scale variability.

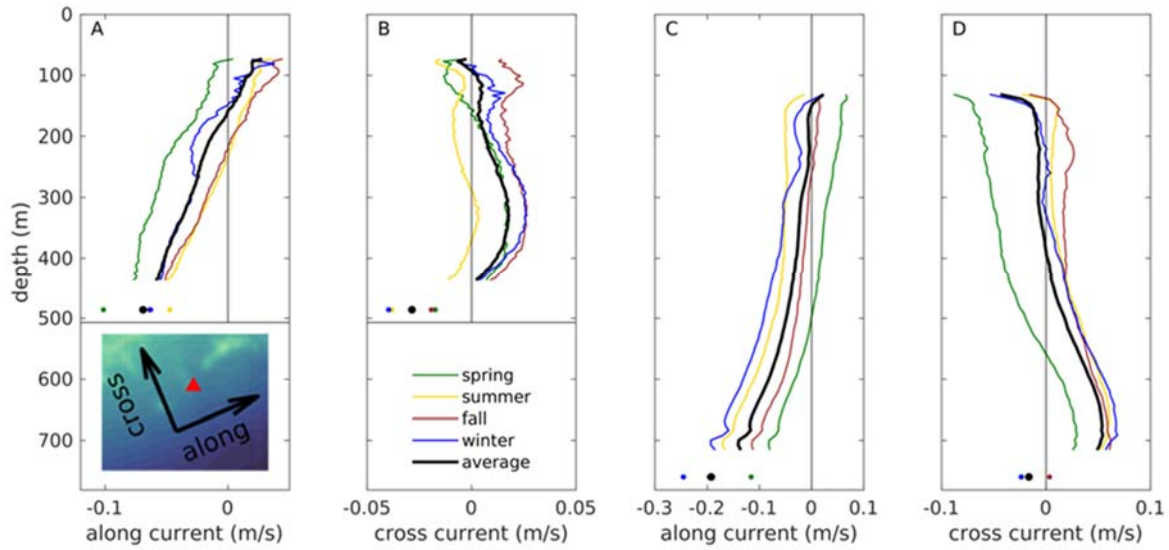

Figure 4.9. A, C) Average along-slope and B, D) cross-slope current profiles using data of the whole respective measurement periods of the long- and short-range ADCPs for (A, B) the Rockall Bank mooring and (C, D) the Oreo Mound mooring. Black lines refer to the annual average, coloured lines to the different seasonal averages. The respective dots indicate the corresponding data from the short-range ADCP (Aquadopp). For a better orientation, the rotated coordinate system from Figure 4.1 is reprinted in A).

At both stations, although more pronounced above Oreo Mound, the decoupling of the currents between the SML and interior is visible at a depth of approximately 150 m in the annual mean current. Below the lower boundary of the dynamic SML, there is an almost homogeneous layer of weak flow in the depth range 150 to 250 m. Already at a depth of approximately 300 m, the south-westward along-slope current (negative sign in Figure 4.9) intensifies and reaches velocity magnitudes of over 0.1 m s^{-1} at 700 m depth. Data from the Aquadopp, deployed closer to the seafloor, suggest that the residual along-slope current is further intensified towards the bottom and reaches approximately -0.19 m s^{-1} in the along-slope direction. The residual cross-slope current exhibits a maximum value of approximately 0.05 m s^{-1} at a depth between 600 and 700 m and is decreasing again towards the bottom. The residual near-bottom currents (especially in the along-slope direction) at Oreo Mound are nearly twice as high compared to current velocity data from the reference site at Rockall Bank (Figure 4.9 D).

The annual depth-integrated current is variable, but the vertical structure of the currents remains similar, which indicates that the structure of the water column as well as the physical processes that govern the flow are stable. The near-bottom along-slope current magnitude above Oreo Mound is relatively high in summer and in winter, but weaker in spring and fall. In the cross-slope direction, the current is rather constant over the year, except for an apparent down-slope flow component over the whole water column in spring. At Rockall Bank, the southward along-slope current is

stronger in spring than during the rest of the year, and the cross-slope component is typically directed up-slope, except for summer when across slopes currents are weaker and partly directed down-slope.

Sediment trap data and fluorescence/turbidity time series

The total mass fluxes on the shallower Rockall Bank were higher than the total mass those at the deeper Oreo Mound. Total mass fluxes on the Bank were around 50 mg d-2 d-1 during summer and fall 2017 and increased sharply to a maximum of almost 900 mg m^{-2} d^{-1} in winter 2018. The maximum mass fluxes corresponded to the time when turbidity and fluorescence signals started to increase (Figure. 4.10 A). At the Oreo Mound total mass fluxes were around 40 mg d^{-2} d^{-1} during summer, while they decreased to around 20 mg m^{-2} d^{-1} during winter and spring 2018 (Figure 4.10 B). Contradictory to the decrease in total mass fluxes during winter times, the fluorescence signal started to increase in both the shallow and deep FLNTU sensors at the Oreo mooring. The fluorescent counts were higher in the shallower sensor but showed the same pattern in the deeper sensor.

At both locations Rockall Bank and Oreo Mound, as well as at both depths shallow and deep at Oreo Mound a temperature decrease was observed in tandem with the fluorescence increase in winter.

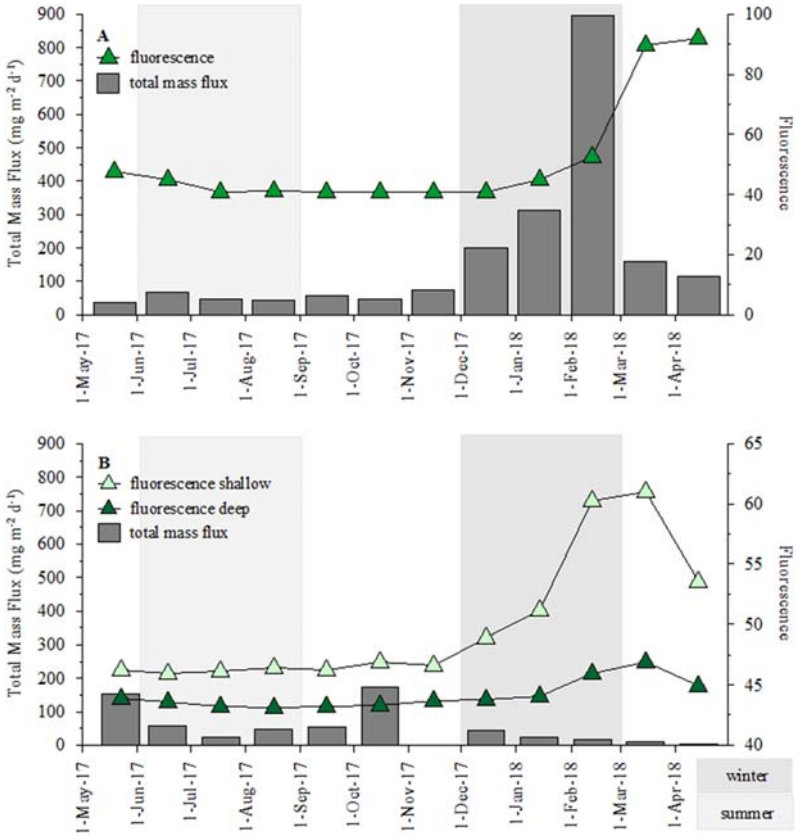

Figure 4.10: Comparison of total mass fluxes (bars) collected with sediment traps and the fluorescence signal (lines) recorded by FLNTUs at A) Rockall Bank and B) Oreo Mound.

Organic carbon and nitrogen

The isotopic composition of organic carbon ($\delta^{13}C_{org}$) and nitrogen ($\delta^{15}N_{tot}$) of the collected material (Figure 4.11) stayed rather constant on the Rockall Bank displaying values of around -22 ‰ for $\delta^{13}C_{org}$ and +4 ‰ for $\delta^{15}N_{tot}$. At the Oreo Mound, however, the values showed a switch to more positive values during winter. The $\delta^{13}C_{org}$ increased from around -22 ‰ during summer to around -18 ‰ during winter, while the $\delta^{15}N_{tot}$ showed an ongoing increasing trend towards more positive values from +3 ‰ in summer to around +9 ‰ during winter. Regarding the contrasting isotopic composition on the Oreo Mound during summer and winter towards more positive values in winter, it suggests that the material on the Oreo Mound is rather recycled during that time, while it remains rather fresh on the Bank.

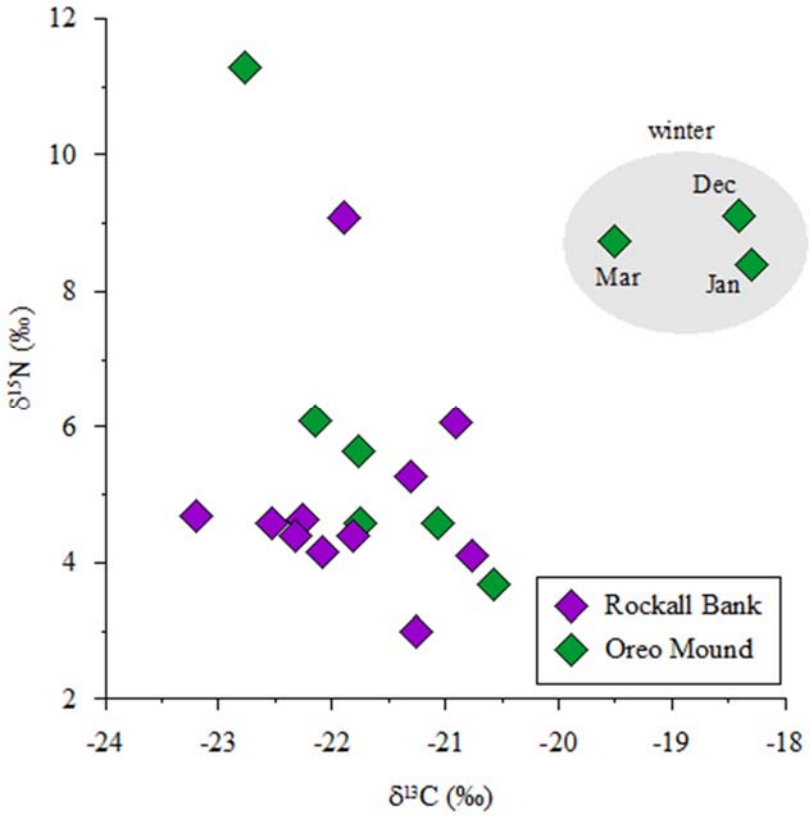

Figure 4.11: Nitrogen ($\delta^{15}N_{tot}$) vs. organic carbon ($\delta^{13}C_{org}$) isotopic composition from material collected at Rockall Bank (purple) and Oreo Mound (green).

Transport of suspended particles

To investigate how the magnitude and direction of horizontal suspended particulate matter (SPM) fluxes are typically distributed, the depth-averaged current velocity data obtained with the Aquadopp and the turbidity and fluorescence data from the FLNTUs (interpolated to the half-hourly

temporal resolution of the Aquadopp) were multiplied to calculate horizontal (point) fluxes. For the shallow sensor at Oreo Mound (from which only fluorescence data is available), the current velocity data from the corresponding vertical bin of the long-range ADCP was used for the calculation. The fluxes were averaged for every 24-hour period to exclude subtidal signals, and the results are displayed in Figure 4.12.

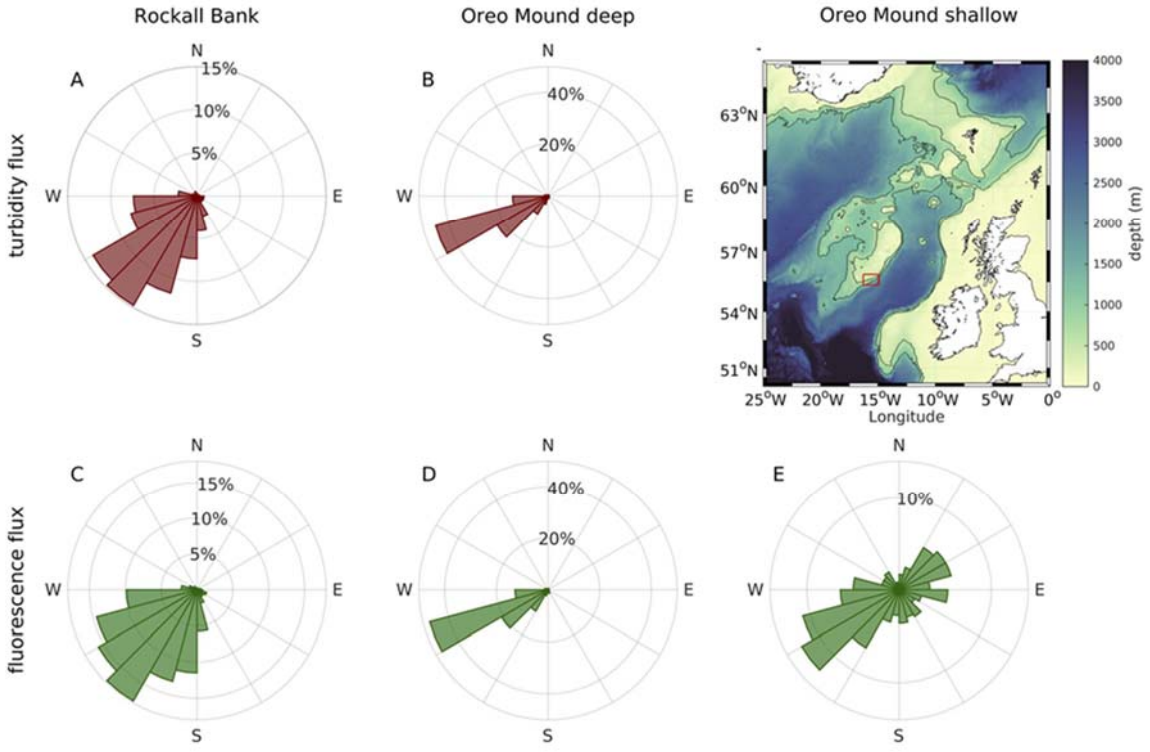

Figure 4.12: Histogram of 24 equally spaced directional bins of the diurnally averaged horizontal fluxes of (A, B) turbidity and (C, D, E) fluorescence for (A, C) Rockall Bank and (B, D) the deep and (E) shallow sensor at the Oreo Mound mooring. The direction of the bins correspond to the direction of the horizontal fluxes. To ease orientation, a map of the study area is displayed in the upper right corner.

Although turbidity fluxes cannot be directly translated to SPM transport, as the underlying quantity for the calculations is turbidity and not SPM concentration, they give a qualitative indication of the transport direction. The transport direction of the deep sensor at Oreo Mound, especially of the higher fluxes, is remarkably narrow-banded, and directed towards the south-west, in line with the direction of the annual mean current. This indicates that a continuous residual transport of SPM and fluorescent material from the north-east towards the south-west takes place in the BBL above Oreo Mound. At Rockall Bank, the main transport direction is, although wider spread, also in a westerly to south-westerly direction.

Indications for WTOW presence

Data from the 24-hour CTD station suggests that the WTOW is not always present above the Oreo Mound (Figure 4.6). This is in line with findings from earlier studies that found WTOW to be present at the latitude of the Extended Ellet Line (57°N) in 75% of the time (Johnson et al. 2010). Unfortunately, the long-term moorings were not equipped with a CTD sensor, but temperature was continuously sampled at 23 m above the seabed (FLNTU sensor). From the 24-hour CTD station at Oreo Mound, a temperature threshold of 8.4°C can be identified to separate the WTOW from the overlying water. With this threshold, it is possible to estimate when WTOW was present above the mound from the temperature time series. The results are displayed in Figure 4.13, along with daily averages of the southwestward along-slope current near the bottom.

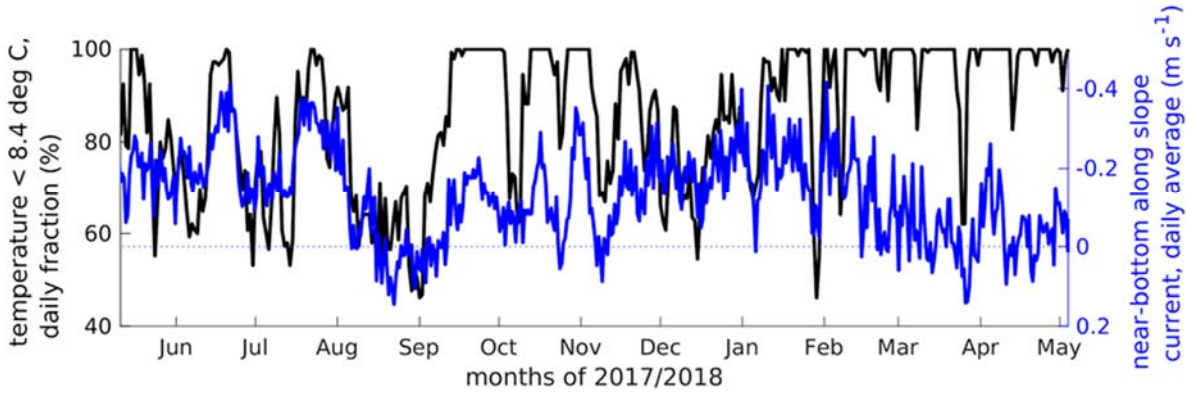

Figure 4.13: Daily fraction of detected temperature values smaller than 8.4°C (black, left vertical axis) and daily averages of the near bottom current (average of the lowermost 5 bins of the long-range ADCP, blue, right vertical axis) at Oreo Mound over the sampling period. Please note that the orientation of the right vertical axis is reversed.

On average, water colder than 8.4°C (here interpreted as WTOW) could be detected in 86% of the (half-hourly) sampling points during the measurement period. This may be a severe overestimation of the presence of WTOW, as other water masses may also be colder than 8.4°C, and we do not have an estimate for a lower bound temperature threshold. However, periods with comparably small presence of WTOW coincide with a weakening of the along-slope near-bottom current (Figure 4.13, blue line), at least during summer, fall and winter (mid-June to beginning of February). This indicates that pulses of WTOW are transported along the eastern side of Rockall Bank, associated with high south-westerly near-bottom currents. During spring, the near-bottom along-slope current is weak compared to other seasons, with a strong return flow near the surface (Figure 4.9 C). Moreover, the cross-slope flow at Oreo Mound has a strong down-slope component above 550 m water depth (Figure 4.9 D). This might be a reason why the presence of WTOW does not coincide with the strength of the near-bottom along-slope flow after February 2018.

Qualitative comparison of observed current data with model results

Due to lack of data from observed currents for the model simulation periods (1978 – 1980, 1992 – 1994), data of observed currents for the present day AMOC state (weak AMOC) was compared with model results for the corresponding weak AMOC state between 1978 and 1980. The first observational data set was collected by NUIG (Ireland) during a 6-week deployment of two current meters in August and September 2000 at depths of 10 and 150 meters above bottom in the Logachev mound province (White et al. 2007). The second data set was collected as part of the ATLAS programme by NIOZ (Netherlands) during a 12-months deployment of two profiling ADCPs in the Logachev mound province on the Oreo Mound (41 m above bottom) and upper Rockall Bank slope (41 m above bottom) (see description above). Table 4.2 summarizes the mooring locations, sampling periods, and respective water depths.

Table 4.2. Summary of locations and sampling periods of current meter moorings used for model validation.

Location	Longitude (W)	Latitude (N)	Sampling period	Water depth	Instrument depth
Logachev	15°27.7’	55°36.4’	02-Aug to 15-Sep 2000	818	808
Logachev	15°27.7’	55°36.4’	02-Aug 2000 to 15-Sep 2000	818	668
Logachev (Oreo mound)	15°51.968'	55°27.048'	09-May 2017 to 05-May 2018	781	740
Rockall Bank (upper slope)	15°55.839'	55°38.448'	02-May 2017 to 05-May 2018	507	466

Three-hour averages (2000 data) and daily averages (2017/2018) were extracted from the model at the locations and depths closest to the mooring locations. Depth-averaged currents were used for the 2017/2018 period. Figure 4.14 (2000 data) and 4.15 (2017/2018 data) show the time series for each east (u) and north (v) velocity component and the corresponding scatter plots, respectively. The comparison suggests sufficient confidence in the model skill to capture the dominant flow patterns at both depth levels over the entire sampling record. The best agreement was found in the

near-bottom layer, where flow dynamics and variability are dominated by tide topography interaction. The comparison between 2017/2018 observed depth-averaged currents and corresponding 1978/1979 model data shows a good representation of the main variability patterns in the model (especially at the upper Rockall Bank slope mooring), but a clear deficit of the model to reproduce the magnitude and occasionally the timing of the observed velocities. This is most likely due a large inter-annual bias introduced by comparing entirely different years. In both periods 2000 and 2017/2018, a generally better agreement between model and observed data was found in the across-slope direction (v-component).

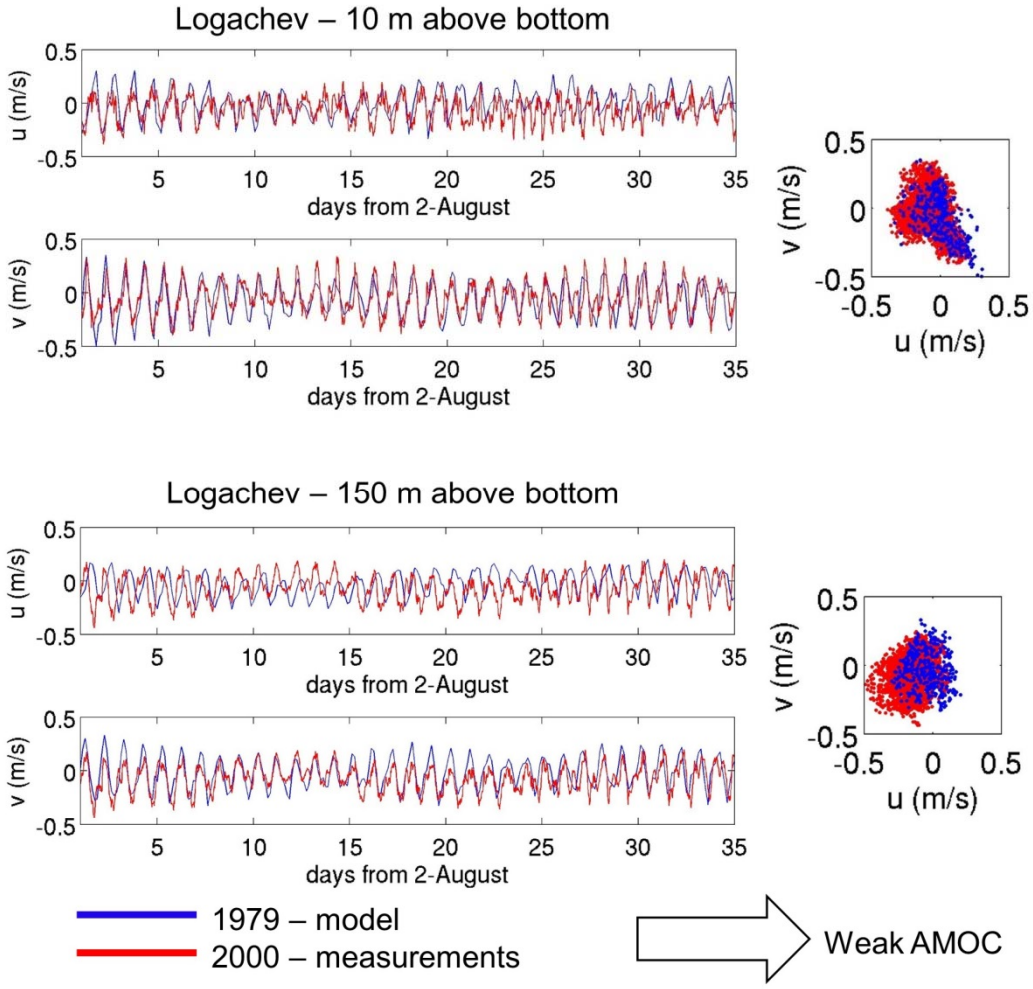

Figure 4.14: 35-day (2nd August to 7th September 2000) time series and scatter plots of observed (red) vs corresponding 1979 modelled (blue) currents at the NUIG Logachev mooring location (see Table 4.2). Top: 10 m above the seafloor. Bottom: 150 m above the seafloor.

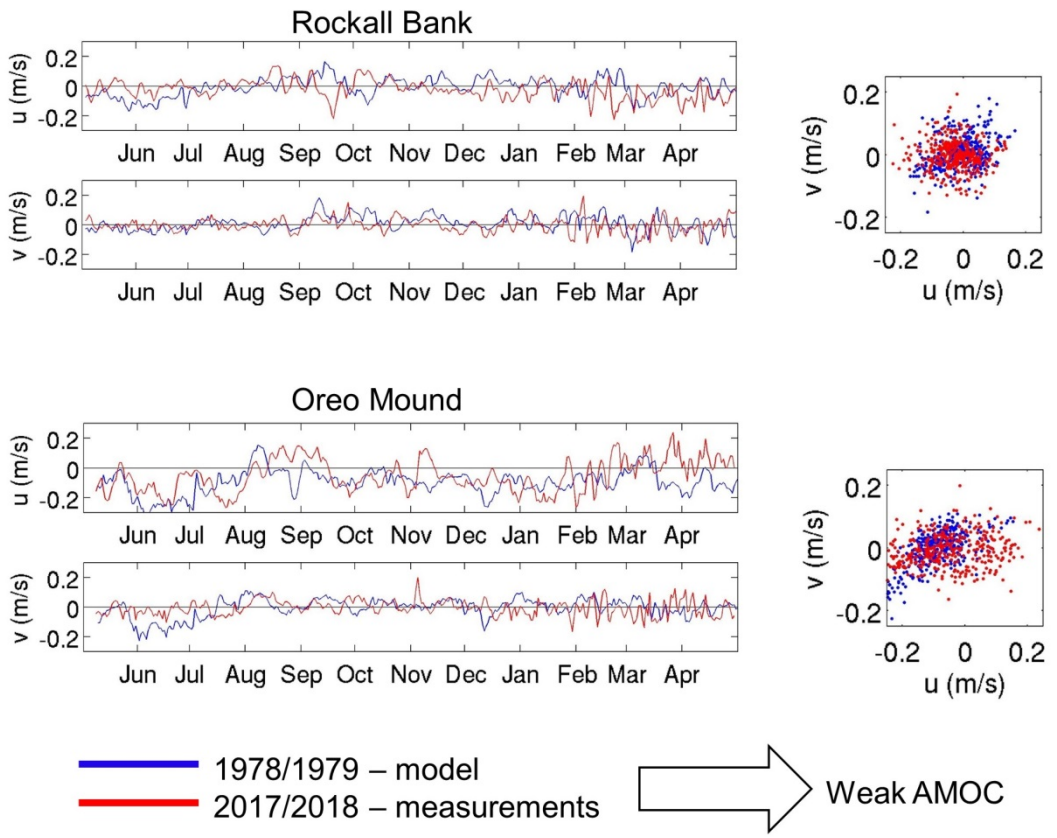

Figure 4.15: 355-day (10th May 2017 to 30th April 2018) time series of observed (red) vs corresponding 1979 modelled (blue) daily averages of depth-averaged currents at the NIOZ mooring locations (see Table 4.2). Top: Upper Rockall Bank slope. Bottom: Oreo Mound.

4.1.4 Discussion

Several hypotheses on the food supply for the cold-water coral mounds in the study area are under discussion. One hypothesis is that the interaction of the tidal currents with the mound itself causes a downward transport of organic matter under spring tide conditions (Soetaert et al. 2016). Monthly averages of the fluorescence signals recorded by the shallower and deeper FLNTU instruments at the Oreo Mound mooring showed a coherent pattern, especially during winter when higher counts were first recorded in the shallower and later in the deeper sensor (Figure 4.10 B). While this observation points to vertical transport of the fluorescent material with a certain degree of degradation from the surface towards the deep, estimates of vertical velocities from the deployed instruments, that are in the range as found in the model by Soetaert et al. (2016), have a large error potential and can therefore not conclusively confirm vertical transport. In addition, the higher fluorescence signal did not result in higher particle fluxes in the trap. The particle fluxes remained rather low and contained a higher isotopic composition (Figure 4.11). This suggests that the material is rather old and recycled instead of fresh material derived from the surface and hence leads to another hypothesis for food

supply towards the Oreo Mound. Duineveld et al. (2007) suggest that organic-rich material from the shallower regions at Rockall Bank is transported by cross-slope advection towards the mound. Data from the CTD transect in May 2017 confirms the existence of a turbid BML above Rockall Bank, in which organic matter could be transported, however this turbid region does not extend all the way to Oreo Mound. This points to the fact, that the material caught during winter at the Oreo Mound is admittedly old but did not necessarily derive from the Rockall Bank mooring location. Horizontal fluxes calculated for the BML at Rockall Bank and Oreo Mound indicate a persistent transport direction towards the south-west (Figure 4.12), yielding that SPM is overall transported rather along-slope than cross-slope. Still, the long-term ADCP data from the Oreo Mound mooring (Figure 4.6 B) also showed a diurnal cross-slope current moving the water masses up- and downslope the mound. Therefore, it is likely that the material caught in the trap at the Oreo Mound is transported in water masses from the northeast that are pushed up and down towards the cold-water corals.

Findlay et al. (2013) discuss potential future scenarios of the well-being of cold-water corals in shallow settings. Considering for example higher sea surface temperatures and shifts in nutrient concentrations that result in primary productivity changes in the surface ocean, it may also directly affect cold-water coral metabolism and functioning. Although strong stratification prevents mixing, sporadic downwelling events may increase temperatures around the cold-water corals to values outside their thermal range of 4-12°C (Roberts et al. 2006). Until now, the consequences are not well understood, but since cold-water corals are also a habitat for other benthic species, it is important to take future changes into account to sustain cold-water coral reefs.

4.2 Condor Seamount

4.2.1 Site description

Condor Seamount is located approximately 17 km southwest of the island of Faial in the Azores Archipelago. It is an elongated seamount centred at 29° W longitude and 38° 32’ N latitude and rises from 1200 (eastern side) to 2000 (western side) m water depth towards a narrow summit plateau (Figure 4.16). The length of the seamount is 35 km, the width is 2 – 6 km, and it is characterized by a diverse benthic landscape (Tempera et al. 2012). The average depth of the main summit plateau is 184 m and the depth range of the summit rim is 250 – 300 m. Condor Seamount is connected to Faial Island by a small sill of approximately 800 m depth. Water masses and currents in the wider Azores region are largely dominated by the Azores Current system and inflow of waters from the subtropical gyre. The Azores Current is one of the most prominent flow systems of the basin-wide circulation in the subtropical Northeast Atlantic. It originates as an eastward flowing branch of the Gulf Stream west of the Mid-Atlantic Ridge, crosses the Mid-Atlantic Ridge between 35°N and 40°N

and continues to flow south-eastward east of the Mid-Atlantic Ridge. The main current is defined as an up to 150 km wide meandering eastward jet in the upper 1000 meters east of the Mid-Atlantic Ridge between the Azores and the island of Madeira (Klein and Siedler 1989, Lozier et al. 1995, Jia 2000). The current's central axis is located around 35° - 40°N latitude with average current speeds of 10 - 20 cm s^{-1} and maximum speeds in the order of 40 – 50 cm s^{-1} (e.g. Pingree 1997). The Azores Current is also an area of intense mesoscale eddy activity. Eddies are formed as a result of baroclinic instabilities of the main Azores Current and propagate inside characteristic corridors (e.g. Alves et al. 2002; Sangrà et al. 2009). In deeper waters, south-westward propagating Mediterranean Water eddies (Meddies) and their pathways along and across complex topographic features including seamounts have been frequently reported (Richardson et al. 2000, Shapiro et al. 1995; Wang and Dewar 2003; Bashmachnikov et al. 2009). Water properties around the Azores archipelago are characterized by the influence of three major water masses (Palma et al. 2012), ENACW (Eastern North Atlantic Central Water, temperature range 10 – 20 °C, salinity range 35.5 – 36.4), MW (Mediterranean Water, 5 – 10 °C, salinity range 35.3 – 35.6) and NADW (North Atlantic Deep Water, 3 – 5 °C, salinity range 34.9 – 35.3).

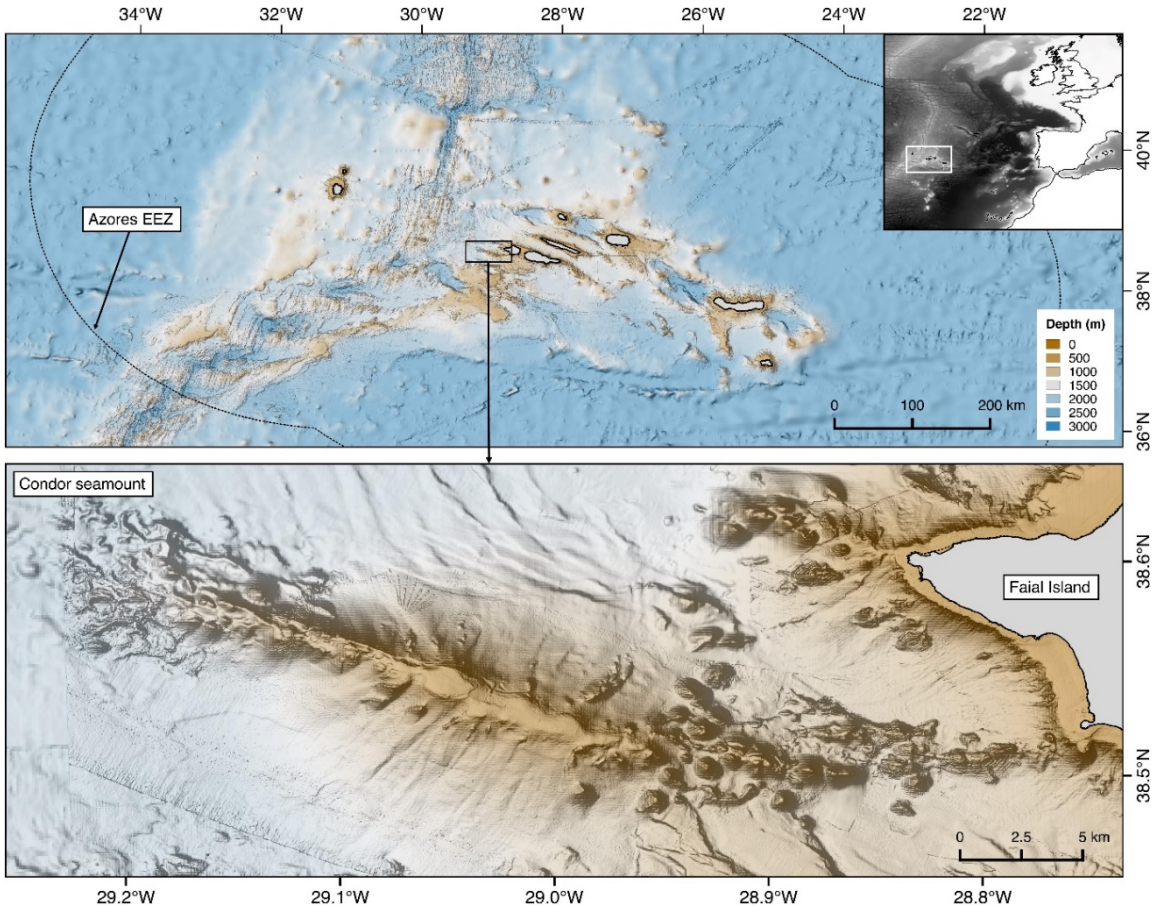

Figure 4.16: Bathymetry of the Azores EEZ (top) and the Condor seamount area southwest of Faial Island based on high-resolution multibeam data collected by IMAR. Coloured contours indicate water depths from shallow (brown) to deep-water areas (blue).

Primary productivity is described to be generally low but show elevated values in spring and can be locally enhanced in areas with strong upwelling around islands and seamounts (e.g. Santos et al. 2013), providing ideal conditions for the colonization by cold-water corals and other suspension or filter feeders such as sponges. Based on historical and present coral records, the Azores have been described to host a particularly high diversity of cold-water corals with 184 species identified to date (Braga-Henriques et al. 2013; Sampaio et al. 2019) with a greater affinity to the Lusitanian-Mediterranean biogeographic region and to a lesser extent to the western North Atlantic. Condor Seamount hosts habitats of high conservation importance including coral gardens and deep-sea sponge aggregations (Tempera et al. 2012). Dense coral gardens dominate the seamount summit area, at water depths shallower than 287 m. The gorgonians *Viminella flagellum* and *Dentomuricea* c.f. *meteor* are the most common and abundant coral species of the summit, forming dense patches alongside the large gorgonians *Callogorgia verticillata* and *Paracalyptrophora josephinae*, the small branching gorgonian of the genus *Acanthogorgia* and hydrarians of the species cf. *Polyplumaria flabellate* and cf. *Lytocarpia myriophyllum* (Tempera et al. 2012). In contrast, sponge aggregations dominated the seamount flanks between 720 – 860 m depth, with the sponges *Pheronema carpenteri* (Hexactinellida) and a wide variety of lithistid sponges frequently reported (Tempera et al. 2012).

4.2.2 Overview of data, instrumentation and quality control

The results reported here are a brief summary largely based on published findings from the Condor observatory project (Giacomello and Menezes 2011, Bashmachnikov et al. 2013) and measurements conducted during the ATLAS project. In this report, we present water column properties from CTD data collected in 2018 on top of Condor seamount by partners IMAR, University of Southern Denmark and University of Liverpool. In addition, ocean currents from long-term measurements at individual mooring locations collected between 2009 and 2010 during the Condor observatory project are described based on the results published in Bashmachnikov et al. (2013). Access to original data from the Condor seamount project was not possible due to existing data sharing regulations. The most comprehensive data set of directly observed ocean currents at Condor Seamount was collected between June 2009 and October 2010. Five current meter moorings were deployed at the slopes and on top of the summit of Condor Seamount during the Condor observatory project. Figure 4.23 and Table 4.3 presents an overview of mooring locations, deployment periods and selected deployment depths according to Bashmachnikov et al. (2013).

Moorings A, B, C and D were fitted with four Anderaa RCM 7 and 8 current meters at various depth levels (see Bashmachnikov et al. 2013 for an overview). Table 4.3 only shows the depth levels

highlighted in Figure 3 of Bashmachnikov et al. (2013), which were used for a qualitative comparison with model data. Data at mooring A (south of the summit) and B (north of the summit) were collected between May 2009 and October 2010, only interrupted by occasional recovery and redeployment of instruments. Moorings C and D were located at the western and eastern rim of the seamount, respectively, and data were collected continuously between March and October 2010. Mooring T was deployed at the summit and collected data with a 300 kHz bottom-mounted, upward-looking ADCP (RDI Workhorse) over a two months period between August and September 2009 at 14 depth levels with 8 m vertical bins.

Table 4.3: Summary of locations, periods and depths of direct current measurements conducted during the Condor observatory project as published in Bashmachnikov et al. (2013). The exact mooring locations were not available, and locations were therefore estimated from published maps.

Location	Longitude (°W)	Latitude (°N)	Sampling period	Water depth estimated from model bathymetry (m)	Instrument depths used for model-data comparison (m)
A (south of summit)	29.058	38.518	May to Nov 2009; Nov 2009 to Mar 2010; Mar to Oct 2010	Approx. 800	200, 250, 400, 800
B (north of summit)	29.030	38.561	May to Nov 2009; Nov 2009 to Mar 2010; Mar to Oct 2010	Approx. 760	135, 200, 400, 755
C (western rim)	29.128	38.566	Mar to Oct 2010	Approx.790	310, 350, 500
D (eastern rim)	28.921	38.498	Mar to Oct 2010	Approx. 780	150, 205, 360, 760
T (summit)	29.030	38.529	Aug to Sep 2009	Approx. 270	180, 200, 220

During the ATLAS project, profiles of different water column properties were collected on top of the seamount at six positions located inside and outside of coral gardens between 6th July and 1st

August 2018. At each station, depth profiles of temperature, salinity and pressure were collected at a resolution of 4 Hz with a CTD90M multi-parameter probe (Sea & Sun Technology, Germany) in combination with additional sensors for profiling oxygen (FireSting O2; Pyroscience), turbidity (Seapoint Sensor Inc., USA), PAR (LI-193SA spherical quantum sensor; Li-Cor Biosciences, USA) and fluorometer (Cyclops-7; Turner Designs, USA). They data were processed and will be added in a later stage as agreed with during the recent meeting with the review panel in Brussels (27th June 2019). Water samples for the characterization of organic matter, nutrients and chlorophyll-a (Chl-a) were collected at 5 m off the Seamount summit (206 - 212 m depth) and in the water column within the Chl-a maximum using a 5L Niskin bottle mounted 2.5 m above the CTD. The CTD profiles were taken before and after each deployment of the aquatic Eddy covariance lander (see D2.3 for results). The depth of the Chl-a maximum was determined based on the Fluorometer depth profile (see Figure 4.17 and Table 4.4 for a summary of 2018 ATLAS CTD and water column sampling stations). The collected depths were averaged from a temporal resolution 4 Hz to a depth resolution of 0.5 m to reduce instrument noise and to allow for a more space-efficient data archiving respectively.

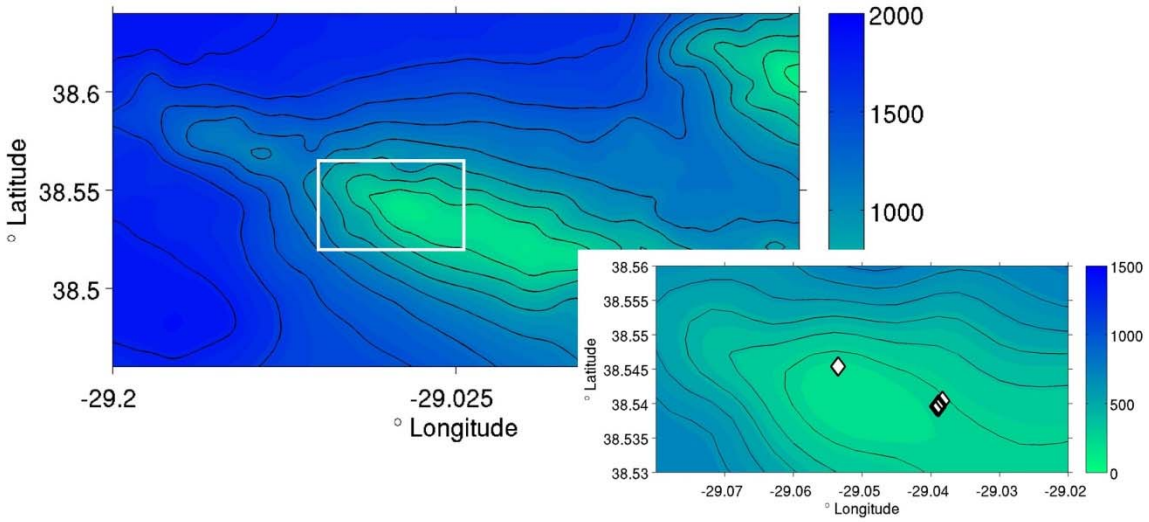

Figure 4.17: Bathymetry of the wider Condor seamount area west of Faial Island. The spatial resolution is 250 m and is based on high-resolution multibeam data collected by IMAR. The black lines show selected depth contours with an interval of 200 m (shallowest area on top of the seamount and west of Faial Island). The zoomed area indicated location of 2018 water column profiling stations collected during ATLAS. Station positions are summarized in Table 4.4.

Table 4.4: Summary of locations, positions and dates of ATLAS 2018 CTD and water column sampling stations at different seamount areas inside and outside coral gardens. AEC refers to the deployment of the Aquatic Eddy Covariance method to measure oxygen fluxes at different locations.

Location	Deployments	Description	Date	Coordinates		Water sampling depth (m)	
Sand	AEC01	Start	06-07-2018	38° 32.7249' N	29° 3.2079' W	207	
		End	09-07-2018	38° 32.7249' N	29° 3.2079' W	207	72
Sand	AEC02	Start	11-07-2018	38° 32.7249' N	29° 03.2079' W	207	
		End	12-07-2018	38° 32.7249' N	29° 03.2079' W	206	78
Mixed garden	AEC03	Start	16-07-2018	38° 32.3813' N	29° 02.3493' W	208	
		End	17-07-2018	38° 32.3813' N	29° 02.3493' W	207	58
Mixed garden	AEC04	Start	17-07-2018	38° 32.3953' N	29° 02.3311' W	207	
		End	20-07-2018	38° 32.3953' N	29° 02.3311' W	207	63
Off garden	AEC05	Start	21-07-2018	38° 32.4221' N	29° 02.2967' W	212	
		End	23-07-2018	38° 32.4221' N	29° 02.2967' W	208	57
Mixed garden	AEC06	Start	24-07-2018	38° 32.3710' N	29° 02.3362' W	209	
		End	01-08-2018	38° 32.3710' N	29° 02.3362' W	211	73

Within the ATLAS project, a sediment trap was moored on the Condor seamount between December 2017 and June 2018 to follow the seasonal dynamics of organic matter fluxes. The sediment trap was

mounted close the seafloor and contained 20 sample jars that were opened and closed following the scheme in Table 4.5.

Table 4.5: Opening and closure dates of the sediment trap mounted at the Condor seamount.

Bottle	Open	Close	Days
1	01/12/2017	01/01/2018	31
2	01/01/2018	01/02/2018	31
3	01/02/2018	08/02/2018	7
4	08/02/2018	15/02/2018	7
5	15/02/2018	22/02/2018	7
6	22/02/2018	01/03/2018	7
7	01/03/2018	08/03/2018	7
8	08/03/2018	15/03/2018	7
9	15/03/2018	22/03/2018	7
10	22/03/2018	29/03/2018	7
11	29/03/2018	05/04/2018	7
12	05/04/2018	12/04/2018	7
13	12/04/2018	19/04/2018	7
14	19/04/2018	26/04/2018	7
15	26/04/2018	03/05/2018	7
16	03/05/2018	10/05/2018	7
17	10/05/2018	17/05/2018	7
18	17/05/2018	24/05/2018	7
19	24/05/2018	31/05/2018	7
20	31/05/2018	08/06/2018	8

4.2.3 Results

Water column structure

Water column properties along individual profiles at Condor Seamount summit in July 2018 are presented in Figure 4.18 (only one profile per deployment is shown for clarity). Water temperature is decreasing with depth, from 21 – 22 °C at the surface to 15 – 16 °C near the bottom. Below a shallow mixed layer in the top 20 m, a sharp thermocline extends from 20 to approximately 50 m depth. Vertical changes in salinity are smaller with the highest values up to 36.3 in the upper 75 m of the water column, decreasing to 36.0 at 200 m depth. Chlorophyll-a levels are lowest close to the surface and close to the bottom. The Chlorophyll-a maximum is located close to, or just below the thermocline with maximum values in the depth range 40 – 100 m. High turbidity values are also confined to the surface layer (top 100 m) with occasionally enhanced turbidity below 150 m depth.

The different water masses at the seamount summit during July/August 2018 hydrographic conditions are highlighted in Figure 4.19. Near-surface water masses at water depths < 75 m are dominated by thermocline waters with a large temperature range (17 – 23 °C), but a rather small range in salinity (36.0 – 36.3). Water masses between thermocline waters (> 75 m) and close to the seafloor (approximately 200 m) are characterized by an almost linear T-S relationship, which can be attributed to the presence of ENACW. ENACW in the Azores regions is the predominant water mass in the upper 600 m of the water column. It originates at a frontal system close to the Azores, which separates high-salinity subtropical ENACW to the south from colder and lower salinity ENACW of sub-polar origin to the north (Rios et al. 1992; Mason et al. 2006). ENACW at Condor Seamount is of subtropical origin, temperatures in July 2018 were in the range 14.5 – 17.0°C, and salinities were in the range 35.9 – 36.4 between the thermocline and 200 m water depth.

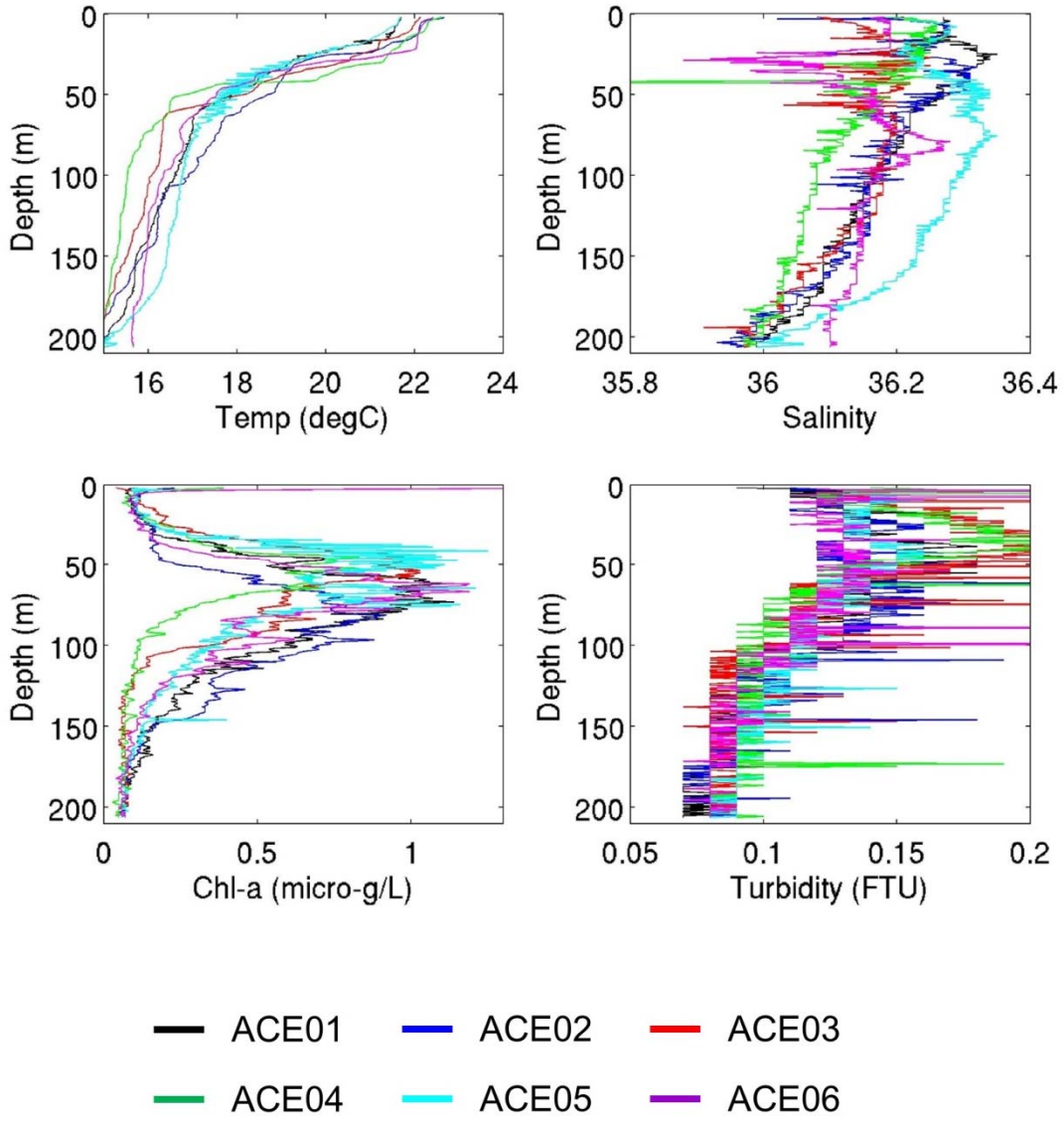

Figure 4.18: Profiles of in-situ temperature (°C), salinity, chlorophyll-a (µg/L), turbidity (FTU) at different stations on top the Condor Seamount summit in July 2018. Colours indicate different deployments (see Table 4.4).

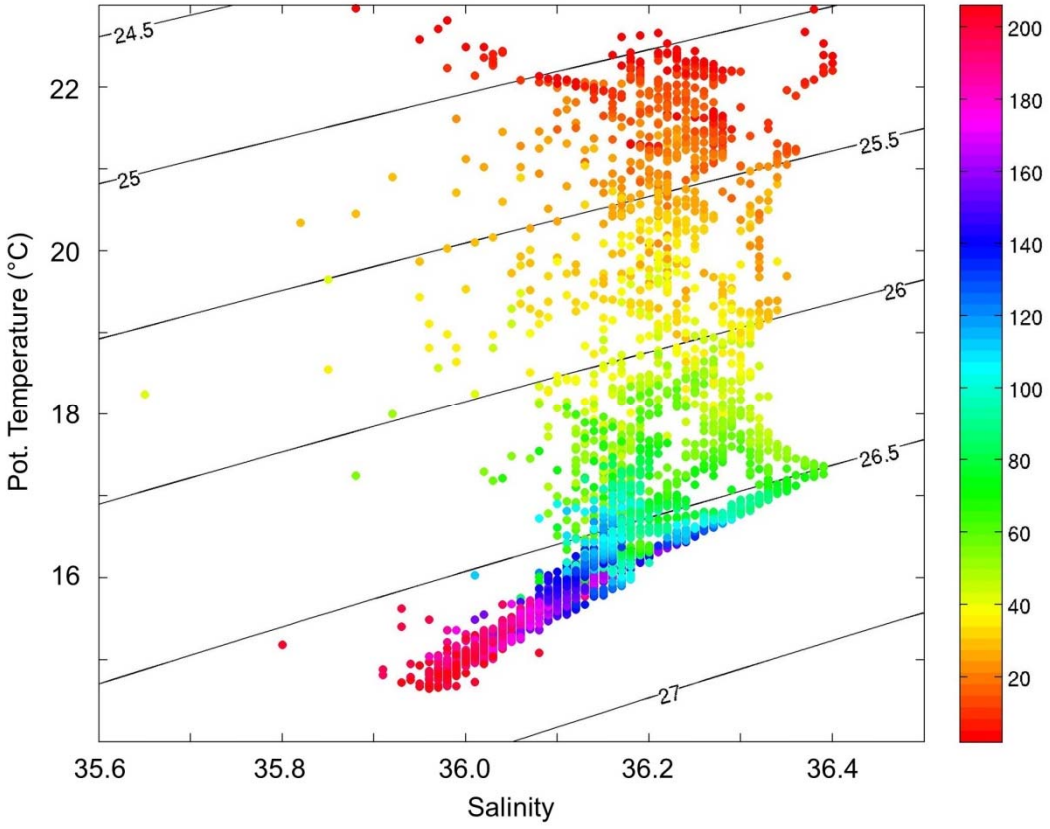

Figure 4.19: T-S diagram highlighting the dominant water masses at Condor Seamount in July/August 2018 based on all CTD profiles shown Table 4.4. Colours indicate different water depths.

Description of flow dynamics at Condor Seamount from Condor observatory results and AVISO data

The description of the predominant circulation features and associated flow dynamics in the Condor Seamount region is based on results by Bashmachnikov et al. (2013) from measurements conducted in 2009/2010, supplemented by an analysis of surface currents from AVISO remote sensing data. The upper-ocean circulation south of the Azores archipelago is dominated by the south-eastward flowing Azores Current system. The main branch seasonally bifurcates east of the Mid-Atlantic Ridge along its south-eastward path (Figure 4.20 and Klein and Siedler 1989). The main branch of the Azores Currents south of the Azores merges with the Canary Current and continues as an energetic southward boundary current east of 25 °W and south of 30 °N (Figure 4.20 and New et al. 2001). The circulation around the Azores Archipelago is dominated by largely southward and south-eastward flow originating from a more northerly branch of Gulf Stream waters crossing the Midatlantic Ridge at 40 °N – 44 °N (Figure 4.20, Figure 4.21 a).

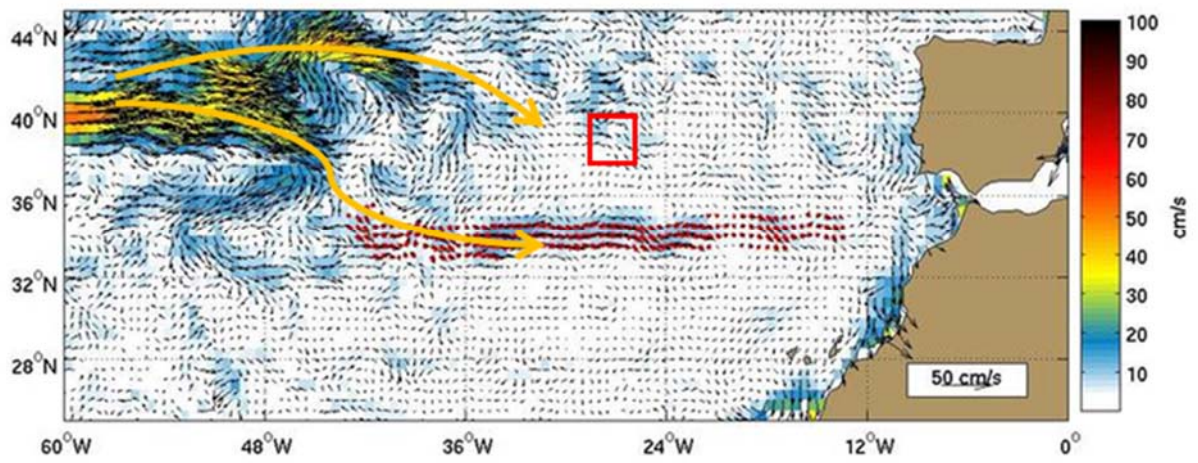

Figure 4.20: Mean ocean surface velocities estimated from drifters (October to December conditions). The figure was obtained from https://oceancurrents.rsmas.miami.edu/atlantic/azores_2.html. Orange arrows indicate the main branches of Gulf Stream waters entering the subtropical North Atlantic east of the Mid-Atlantic Ridge. The red square shows the location of the Azores archipelago.

Mean current speeds vary between 0.06 ms^{-1} in waters close to the archipelago and between 0.1 and 0.15 m s^{-1} in waters further offshore (Figure 4.21 a). Inside and close to the archipelago, variability of surface currents is significantly lower than in more open surface waters away from the archipelago (Figure 4.21 b).

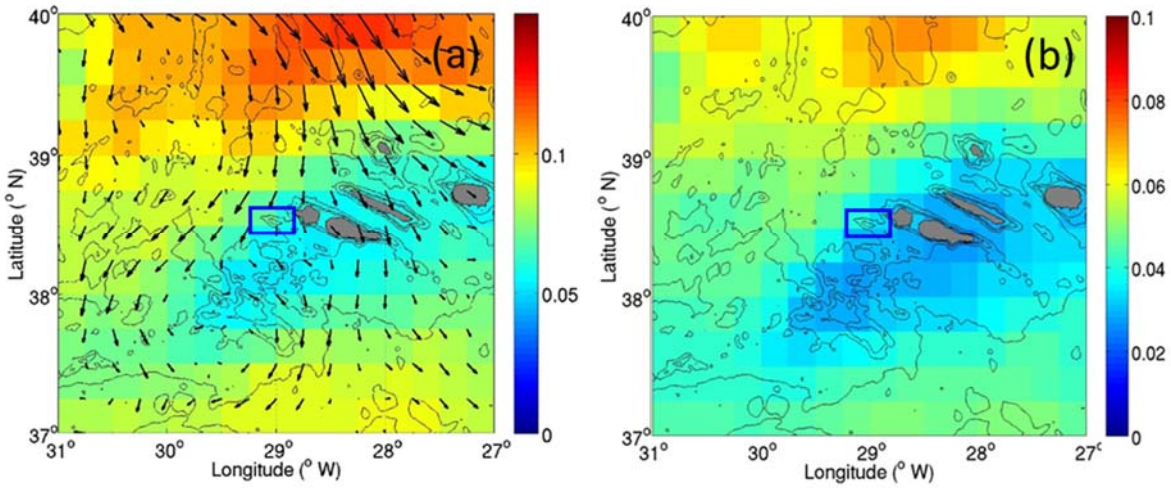

Figure 4.21: Mean surface currents (m s^{-1}) based on monthly AVISO geostrophic currents between 2000 and 2017. (a) Current speed (m s^{-1}, colours) and direction (vectors), (b) standard deviation (m/s). The blue square indicates the location of Condor Seamount.

An extensive and systematic analysis of mean and higher frequency currents based on 1.5 years of moored current meter observations at Condor Seamount revealed a large spectrum of dynamical current patterns and processes (Bashmachnikov et al. 2013). The local dynamical response of flow

over isolated topography such as seamounts depends on a large number of factors including shape and size of the seamount, seamount latitude and frequency of the impinging currents (e.g. Lavelle and Mohn 2010). One of the most common concepts of steady flow over a seamount is known as a Taylor cap, an isolated region of bottom-intensified flow above the seamount accompanied by a dome of cold water entrapped above the summit (e.g. Lavelle and Mohn 2010). Oscillatory flow such as barotropic tides and inertial waves interacting with seamounts generate energetic seamount trapped or freely propagating internal waves, tidally rectified flows and local turbulence. The local dynamical response to oscillatory impinging flow is determined by the inertial frequency (seamount latitude). The Condor observatory 2009/2010 current measurements indicated the presence of a Taylor cap during at least half of the time (Bashmachnikov et al. 2013). The Taylor cap was manifested as an anticyclonic vortex shifted to the southern part of the elongated seamount summit. The time-mean flow followed the bathymetry of the seamount in a clockwise sense with typical velocities of up to 5 cm s^{-1} in the upper 400 m (Figure 4.23). Along the northern summit, the mean flow was to the northwest within the same depth range but turned northeast at near-bottom depths. The mean flow was largely across isobaths to the on top of the seamount in the depth range 180 to 220 m (Figure 4.23). The results suggested three mechanisms for generating and maintaining the anticyclonic vortex over Condor Seamount, i.e. steady impinging mean flow, tidal rectification and vertical turbulent density fluxes (see also Figure. 4.22, copied from Bashmachnikov et al. 2013). The relative importance of the different components of tidal and sub-tidal flow was difficult to estimate, but tidal rectification was suggested as the most important contributor. The stability of the vortex was to a large degree controlled by variability of the large-scale flow field in the immediate far field of the seamount. Periods, during which the vortex was absent, were characterized by pronounced short-term variations in the direction of the impinging larger scale flow (Bashmachnikov et al. 2013). The anticyclonic vortex was re-established after reconsolidation of the mean flow. In conclusion, the largely tidally driven flow dynamics at the seamount were occasionally modulated by variability of the far field flow.

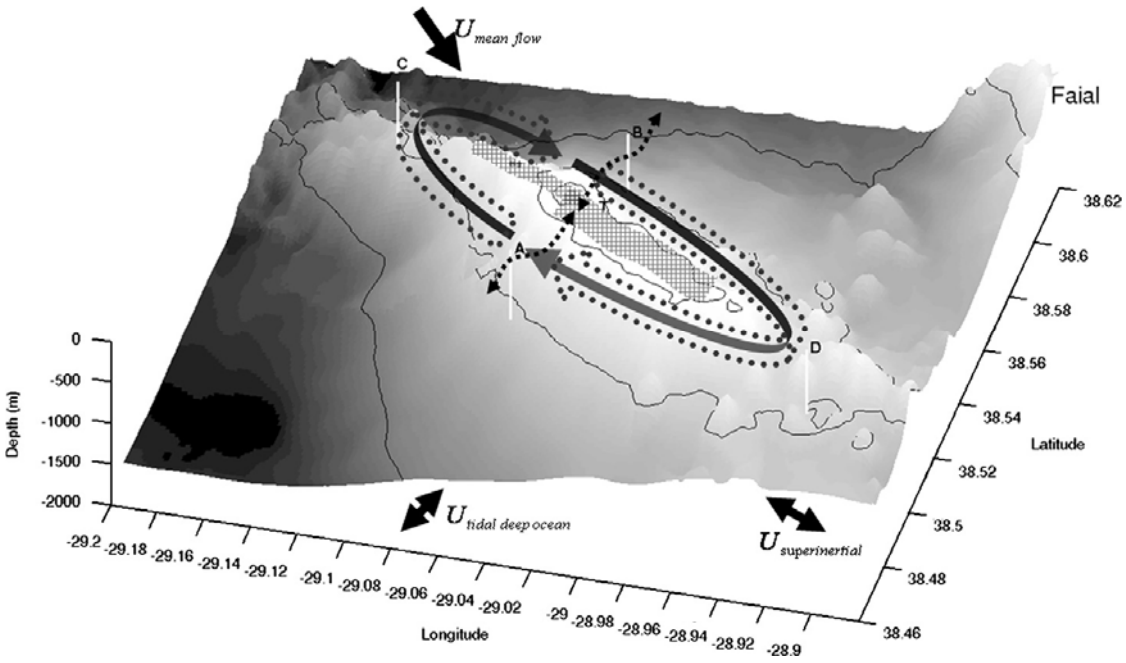

Figure 4.22: Summary of oceanographic conditions at Condor seamount from direct current measurements from 2009 and 2010 (Figure 11 in Bashmachnikov et al. 2013). The dominant drivers of seamount dynamics include the impinging steady far-field flow (U_{mean}), the barotropic tidal flow (U_{tidal}, increasing near the summit) and an oscillatory super-inertial flow ($U_{superinertial}$). The secondary circulation showed enhanced tidally induced upward vertical density flux in hatched areas. The anticyclonic vortex over the summit was shifted towards the southern part of the seamount summit. Black contour lines indicate the 200, 300, 800 and 1500 m depth lines (smallest values at the seamount summit).

The analysis of currents in the tidal frequency spectrum showed two remarkable features. Close to the summit (moorings A, B, T) the tidal signal was dominated by strongly amplified semi-diurnal baroclinic tides. Strongest magnitudes of 10 – 15 cm s^{-1} were recorded for the M_2 tidal constituent at the summit mooring T in the upper 150 – 200 m with a maximum tidal current magnitude of 18 cm s^{-1} measured 40 m above the seabed (Bashmachnikov et al. 2013). This area was identified as the main generation site of energetic semi-diurnal internal waves freely propagating away from the seamount summit into the surrounding oceanic far field (Bashmachnikov et al. 2013). Secondly, a strong amplification of the main diurnal tidal constituents K_1 and O_1 was recorded along the summit rim and over the summit. Here, diurnal tidal currents were amplified 2 – 5 times (K1) and 9 times (O1), respectively, when compared to typical values away from the seamount. This strong diurnal tidal amplification was considered as an important driver for generating and sustaining the described Taylor cap for at least an extended period of time (Bashmachnikov et al. 2013).

Qualitative comparison of model results with results from observed Condor observatory currents

The lack of direct current measurements for the model simulation periods (1978 – 1980, 1992 – 1994) was a limiting factor for evaluating model skill at Condor seamount. Thus, results from the Condor observatory measurements (obtained during a weak AMOC state, see Figure 2.2) were compared with model results for the weak AMOC year 1979. As indicated earlier, the original Condor seamount data were not available for a direct, analytical model-data comparison due to data sharing policy restrictions. Therefore, a qualitative estimate of the model skill was carried out by comparing model data at positions and depths closest to the mooring locations and instrument depths for a specified period with published results in Bashmachnikov et al. (2013). The chosen model period was March to October 1979 (March to October data was also available at moorings A – D in 2010). At mooring T, model data was extracted for the August to September 1979 period only (we used the same year again to allow for a consistent estimate).

The procedure involved two steps: First, we visually extracted vectors of mean current velocities at each depth and mooring location from Figure 3 in Bashmachnikov et al. (2013). Second, model velocities (daily averages) were extracted at the corresponding depths and locations for the period March to October 1979 (weak AMOC state, same as in 2010) and time-averaged mean current velocities were calculated. The result of this qualitative comparison is summarized in Figure 4.23. Agreement between modelled and observed mean currents at Condor observatory mooring locations A – D at the flanks of the seamount can be considered as close to observations, both in magnitude and direction, despite the rather coarse and likely biased methodology. The comparison suggests sufficient confidence in the model skill to capture the dominant flow patterns at different depth levels along the seamount slopes. A less satisfying model skill was found at the mooring T location on top of the seamount summit. In summary, the model showed a good skill of reproducing observed mean currents along the seamount slopes but demonstrated a deficit in reproducing the magnitude and direction of currents at the seamount summit location. It is important to note that this comparison is based on a very basic methodology and will benefit from a more accurate skill assessment, once the Condor observatory data will become open to the public. It is, however, uncertain at this stage, whether Condor observatory data will be released to the public within the lifetime of the ATLAS project.

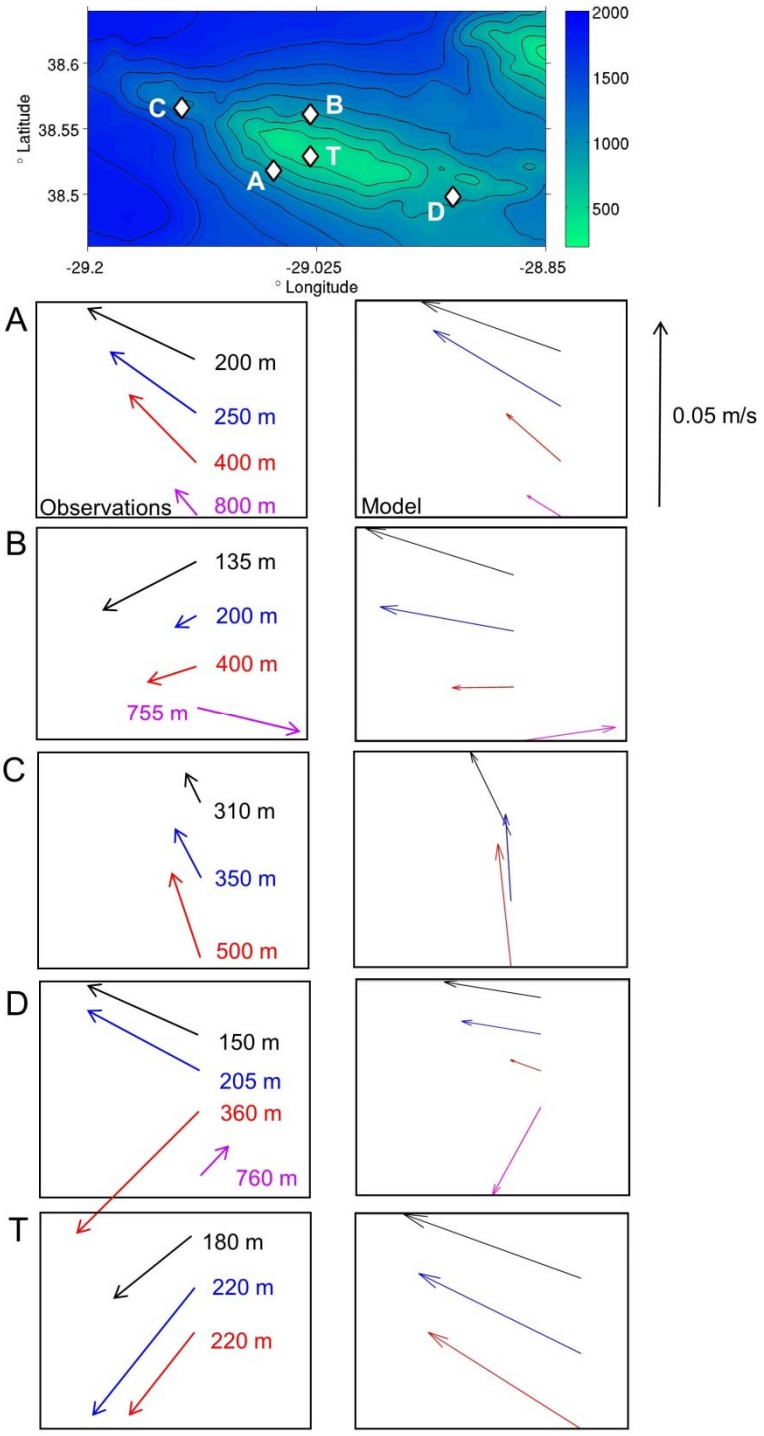

Figure 4.23: Comparison of observed modelled currents at the location of five current meter moorings deployed during the Condor observatory project. The observed current vectors were re-drawn from results published in Figure 3 of Bashmachnikov et al. (2013). Model data were extracted at depths and positions closest to the corresponding mooring depths and positions. Observed mean currents were calculated from data obtained in the period July 2009 - October 2010 (weak AMOC state). Modelled mean currents were calculated for the period March to October 1979 (weak AMOC state).

Sediment traps

The mass flux at Condor seamount averaged at 0.45 mmol N m^{-2} d^{-1} and 0.059 mmol N m^{-2} d^{-1} and showed a pronounced seasonal cycle (Fig. 4.24). Winter fluxes are comparatively low during winter until mid-March (<0.3 POC and <0.04 PON mmol m^{-2} d^{-1}), fluxes remain elevated until mid-May after which fluxes return back to late winter values. The molar C:N ratio was very constant throughout the year (Fig.) and a regression between PON and POC flux was highly significant and indicates a C:N ratio of 7.8±0.22 (mean±se, p<0.001), which is indicative of relatively fresh organic matter.

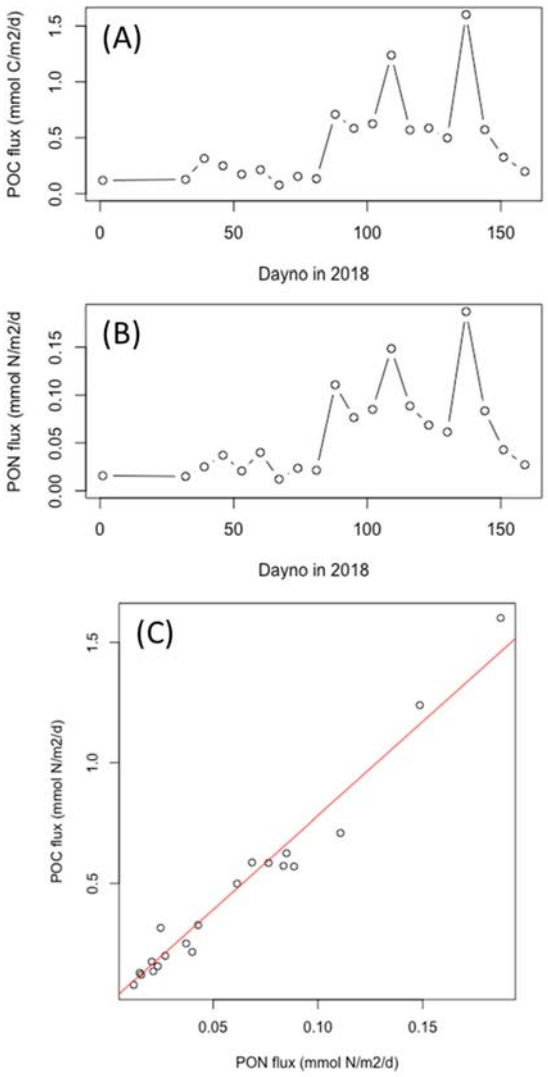

Figure 4.24: (A) POC and (B) PON mass fluxes (mmol m^{-2} d^{-1}) measured on the Condor seamount. (C) Relation between PON and POC flux for all samples.

4.2.4 Discussion

Biophysical coupling at shallow seamounts has often been discussed in the context of tracer retention inside stable Taylor caps accompanied by enhanced primary and secondary production. However, effects of seamount flow dynamics on biological distribution patterns takes many forms (Genin 2004; Genin and Dower 2007) including retention and loss of passive planktonic particles, increased suspension of sediments by elevated turbulence and current shear at the seamount bottom boundary layer supporting food supply to suspension feeders like corals and sponges, to only mention a few. The general assumption of enhanced and persistent aggregation of biological material over seamount summits, however, is often not supported by observations and strongly varies between seamounts. At Condor seamount, Bashmachnikov et al. (2013) largely exclude the potential to enhance primary production over the summit, as the Taylor cap is confined to depths deeper than 170 m, well below the euphotic zone and the seasonal thermocline. Santos et al. (2013) who could not find evidence of increased phytoplankton concentrations at depths < 100 m above Condor seamount confirmed these results. In contrast, there was clear evidence of strong acoustic backscatter over the summits of Condor seamount, which could be attributed to the presence and retention of resident micronekton (Cascão et al. 2017). These are not necessarily contradicting results – previous findings have highlighted the importance of swimming micronekton for maintaining seamount-associated population distributions (e.g. Wilson and Boehlert 2004). The episodic shedding and establishment of the Taylor cap reported at Condor seamount may support trophic enrichment over the seamount by enhanced horizontal fluxes of planktonic prey towards the seamount originating from the far field, a process often referred to as trophic subsidy (Genin and Dower 2007). The combination of energetic internal tides and associated local mixing ensures an important, high quality food source (sediment trap data) for filter feeders atop the Condor summit and along the upper seamount flanks.

4.3 Davis Strait

4.3.1 Site description

Davis Strait is an approximately 400 km wide and 60 km long strait between Baffin Island to the west and western Greenland to the east (Figure 4.25). Davis Strait separates the deep basins of Baffin Bay in the Arctic Ocean (maximum depth 2900 m) and northern Labrador Sea in the north-western North Atlantic with water depths > 3000 m. The shallowest part of Davis Strait is an approximately 640 m deep sill, which prevents exchange of deep waters between the two basins. Water mass transport through the strait is strongly controlled by topography with flow to the north on its eastern side and flow to the south on its western side (Tang et al. 2004, Curry et al. 2014). The larger-scale circulation

between the northern Labrador Sea and the Baffin Bay follows a cyclonic sense (counter-clockwise) and is intensified along the western boundary (Figure 4.25, Curry et al. 2014). The eastern boundary of the Davis Strait is dominated by a combination of the West Greenland Current (WGC) on the Greenland shelf and the West Greenland Slope Current (WGSC) originating in the northern North Atlantic (Figure 4.25, Curry et al. 2004). The two currents carry low salinity (WGC) and high salinity (WGSC) water northward along the eastern Davis Strait, which eventually is entrained into the southern recirculation towards the western boundary of Davis Strait and in the Baffin Bay (Figure 4.25). The WGC is an extension of the East Greenland Current (EGC) with substantial supplies from the EGC coastal inflow and glacial runoff (Sutherland and Pickart 2008). The arctic outflow along the western boundary of Baffin Bay and Davis Strait (Baffin Island Current – BIC) merges with the outflow from Hudson Strait and the westward retroflection of a substantial fraction of the WGSC to feed the southward flowing Labrador Current (e.g. Straneo and Saucier 2008).

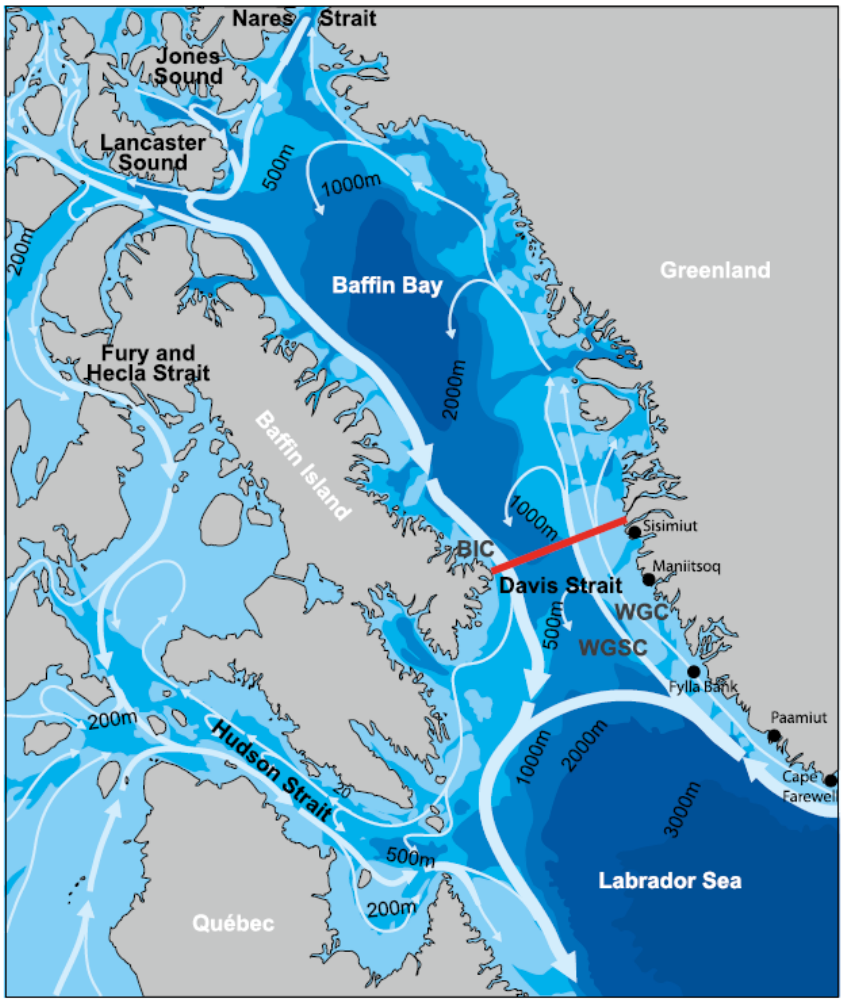

Figure 4.25: General circulation in Baffin Bay, Davis Strait and north-western North Atlantic southwest of Greenland (white arrows). The figure is copied from Curry et al. (2014). Abbreviations: BIC – Baffin Island Current, WG – West Greenland Current, WGSC – West Greenland Slope Current.

The marine shelf regions close to the shelf breaks and the slopes of Baffin Bay, Davis Strait and Labrador shelf host species-rich assemblages of Geodia sponges (see Figure 4.26, Knudby et al. 2013, Kenchington et al. 2010). These assemblages cover a large depth range (200 – 1800 m) and are often aligned along depth contours, where environmental conditions support and sustain growth (Hogg et al. 2010, Murillo et al.2012, Knudby et al. 2013).

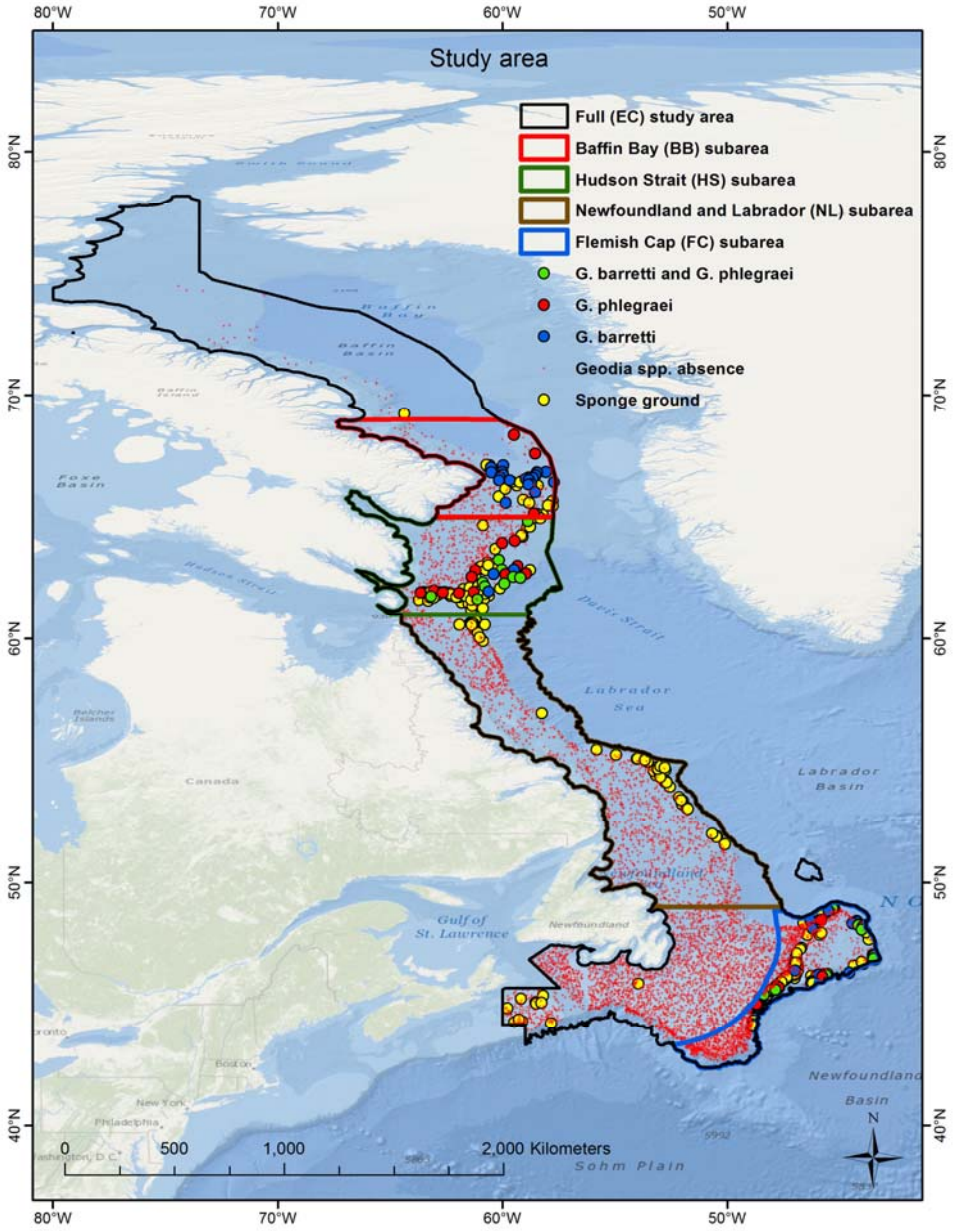

Figure 4.26. Locations of presence and absence data on Geodia sponge grounds with unidentified species. The figure was copied from Knudby et al. (2013). Sponge presence/absence locations are based on research trawl surveys conducted by Canada and EU vessels (see Knudby et al. (2013) for information that is more detailed).

4.3.2 Overview of data, instrumentation and quality control

The results reported here are based on CTD measurements conducted in summer 2018 during the ATLAS project cruise on board the research ice breaker CCGS Amundsen operated by Amundsen Science in Canada. Profiles of water column properties pressure, depth, temperature and salinity were obtained from CTD surveys at 10 positions along two transects perpendicular to the Labrador shelf break (see Table 4.6 and Figure 4.27). The northern transect was located inside a sponge area, whereas the southern transects was located inside an area without sponges. The measurements were carried out between 27-August and 3-September 2018 using a Seabird SBE 9 CTD system. The ATLAS CCGS Amundsen data are supplemented by an analysis of AVISO sea surface geostrophic currents and a summary of results from a report on ocean currents and sea ice statistics for Davis Strait from multi-year records from moored instruments collected between October 2004 and September 2011 (Wu et al. 2013). The ATLAS field programme in the Davis Strait case study area is still ongoing and additional data are collected during an upcoming 2019 CCGS Amundsen cruise. As agreed during the 2nd Review panel discussion on 27th -June 2019 in Brussels, relevant data that will become available after retrieval of the landers will be appended to this deliverable.

Table 4.6: Summary of locations, positions and dates of ATLAS 2018 CTD water column profiling at different positions perpendicular to the Labrador shelf break.

Station number	Date	Depth (m)	Longitude	Latitude
20	27-07-2018	294	-62.9002	59.4003
22	28-07-2018	198	-61.0217	59.3112
23	28-07-2018	614	-60.2678	59.3825
24	28-07-2018	1943	-59.4423	59.4748
25	29-07-2018	2568	-58.6342	59.5337
28	30-07-2018	365	-62.1203	60.4597
29	30-07-2018	396	-61.2938	60.4675
33	02-08-2018	1883	-60.3802	60.4668
34	03-08-2018	2434	-59.2573	60.4685

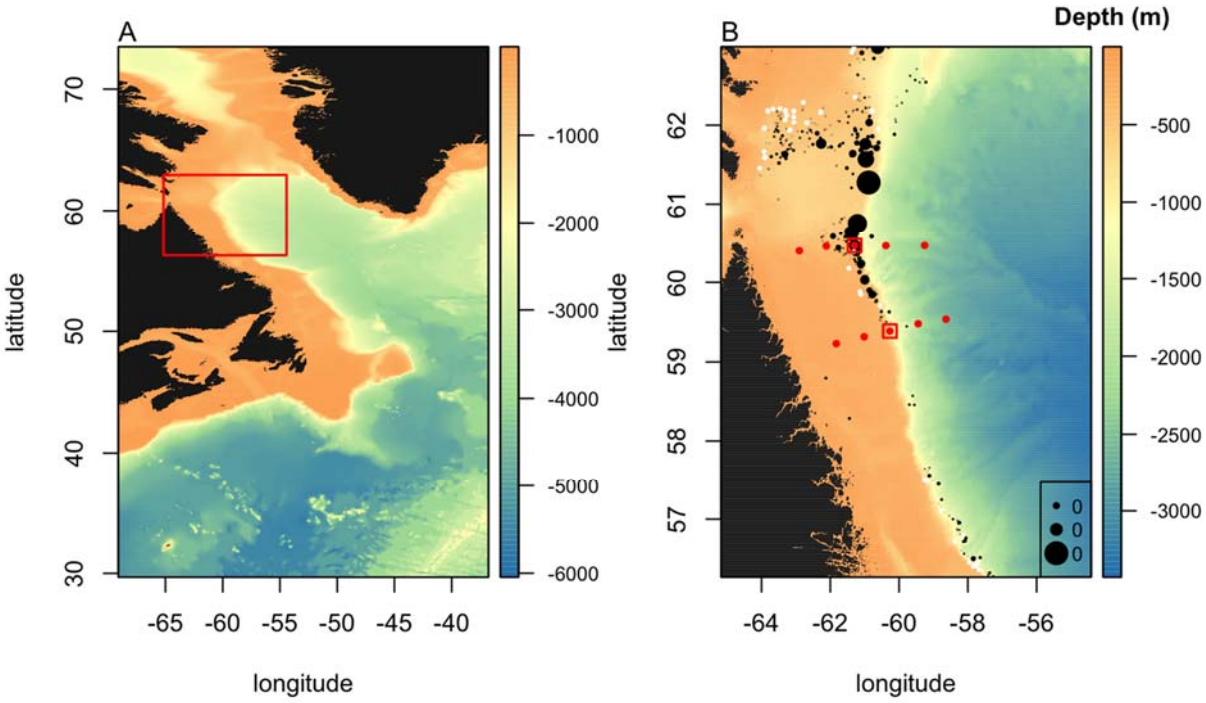

Figure 4.27: (A) Location of the Davis Strait case study area and (b) location of CTD stations along two transects during the summer 2018 CCGS Amundsen expedition.

4.3.3 Results

Water column structure

Water column properties along individual profiles across the Labrador shelf break in July/August 2018 are presented in Figure 4.28 (only the top 600 m of the water column are shown for better visibility). A prominent feature in water temperature profiles was a sharp thermocline in the depth range 10 – 30 m separating warmer surface waters from colder subsurface waters. The subsurface waters in the depth range 40 – 150 m form the coldest water layer at all locations with temperatures of < 0 °C on the shelf (40 – 150 m), 0 – 1°C over the shelf break (40 – 100 m) and 3 °C in deep waters (40 – 80 m), respectively. Temperatures in deep waters below 600 m water depth were between 2 and 4°C (Figure 4.28). Salinity values generally increased with depth but showed a pronounced cross shelf gradient in the upper 200 m. Salinities increased from < 32 on the shelf to almost 34 in open waters east of the Labrador shelf break. At greater depths, salinity changes were small and increasing with depth at values between 34.9 and 34.95.

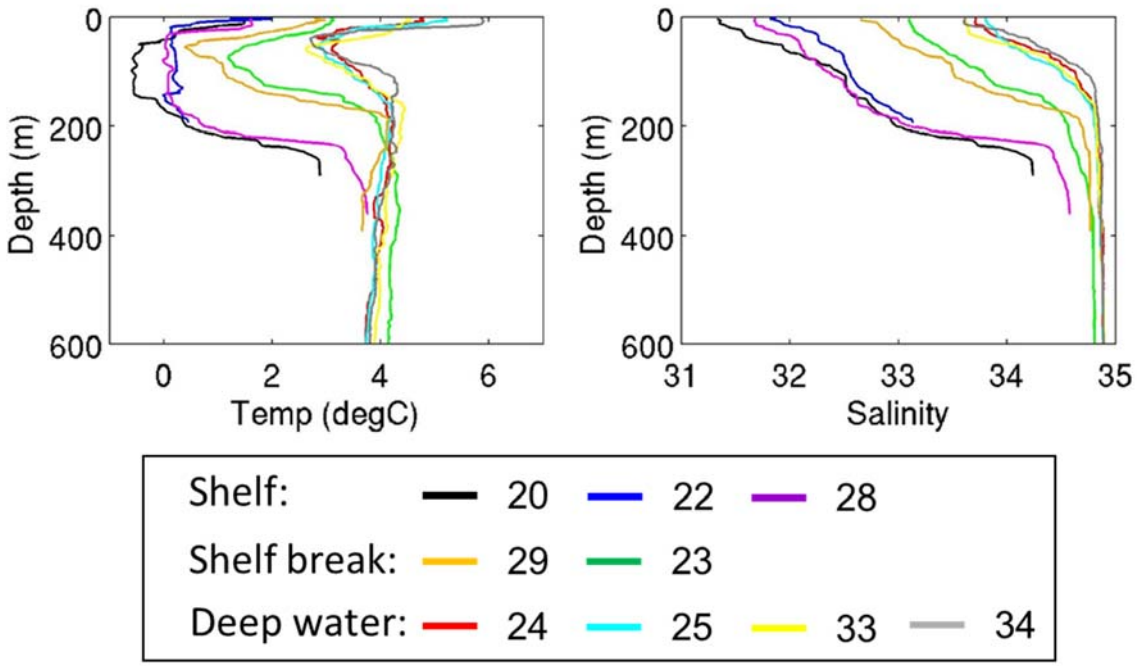

Figure 4.28: Profiles of in-situ temperature (°C) and salinity at different stations along two transect across the Labrador shelf break in July/August 2018. Colours indicate different stations (see Table 4.6).

The water masses at different stations along the two transects surveyed in July/August 2018 are presented in Figure 4.29. The water masses in the case study area have two principal sources – the outflow from the Davis Strait with contributions from Hudson Strait and Atlantic waters from the WGC retroflection. The cold, low salinity upper layer water mass on the shelf is often referred to as Arctic Water and is marked by a distinct temperature minimum in the upper 200 m (e.g. Tang et al. 2004). In our case study area, it is strongly modified by waters of the Hudson Strait outflow, freshwater input from rivers and sea ice melt resulting in low salinities < 33 (Straneo and Saucier 2008, Figure 4.29 a). The influence of warmer and higher salinity waters of Atlantic WGC waters is a distinct feature at the shelf break and over deeper waters leading to higher temperatures (up to 5 – 6 °C) and salinities ≥ 34 in the upper 300 m (Figure 4.29 a). The dominant intermediate water mass is Labrador Sea Water (LSW), which characterized by cold water and relatively low salinity compared to surrounding waters. The LSW salinity minimum in summer 2018 was 34.87 at 1100 m depth (Figure 4.29 b). The increase in salinity below LSW depths can be attributed to the presence of North Atlantic Deep Water (NADW) in the depth range 1300 to 2000 m (Figure 4.29 b).

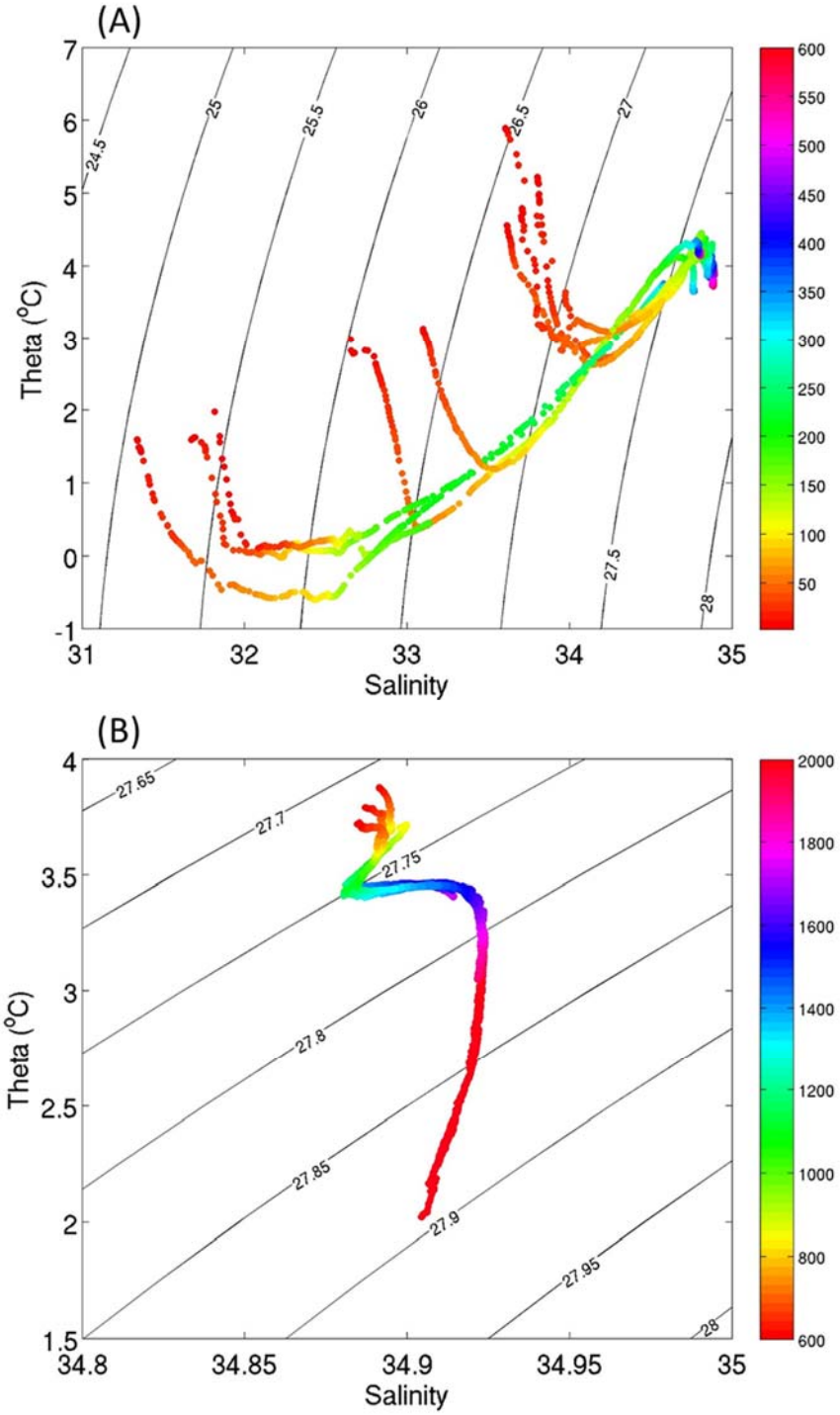

Figure 4.29: T-S diagram highlighting the dominant water masses in the Davis Strait case study area in July/August 2018 based on all CTD profiles shown Table 4.5. (A) Water masses in the depth range 0 – 600 m, (b) water masses at depths > 600 m. Colours indicate water depths.

Description of major circulation features based on literature and AVISO data

The large-scale circulation through the Davis Strait is dominated by a poleward flow of Atlantic water into the Baffin Bay and a return flow of modified Arctic water out of Davis Strait into the Labrador Sea. Long-term current measurements between 2004 und 2011 conducted along a transect between Greenland and Baffin Island recorded the strongest flow velocities within the outflow from Davis Strait and a substantial seasonal variability of the entire system (Wu et al. 2013). Near-surface annual averages varied between southward flow of 0.15 m s^{-1} along Baffin Island to northward flow of up to 0.08 m s^{-1} along western Greenland (Wu et al. 2013). There was a pronounced seasonal variation in current magnitude with strongest currents in summer and fall when compared to winter and spring (Wu et al. 2013). Long-term mean surface currents in the Labrador Current south of 62°N between 2000 and 2018 from AVISO remote sensing data were as high as 0.3 m s^{-1} (Figure 4.30 a). Currents of similar magnitude could be found inside the WGC system around southwest Greenland. Flow variability in these current systems is also highest when compared to the southern and central Davis Strait (Figure 4.30 b). Other areas of enhanced flow magnitudes and variability include the Davis Strait outflow and the poleward flow of WGC and WGSC waters along the Greenland coast. Tidal currents in Davis Strait were found to be strong with magnitudes close to or exceeding the residual (non-tidal) flow (Wu et al. 2013). Semi-diurnal tidal currents are dominant contributor to the tidal spectrum in Davis Strait with highest magnitudes recorded for the M_2 tidal constituent, except in near-coastal waters, where diurnal tidal currents can be of similar magnitude than the semi-diurnal tidal currents (Wu et al. 2013). The Labrador Current, a western boundary current system extending from the surface to water depths of > 2000 m, dominates the along-slope flow south of 60 °N. The variability of the deep Labrador Current is strongly linked to decadal variability patterns of ocean-atmosphere heat flux (controlling deep convection in the Labrador Sea) and wind stress (Dengler et al. 2006, Böning et al. 2006). Dengler et al. (2006) reported a strengthening of the deep Labrador Current of 10 to 20% from the late 1990s to the years after 1999. Fischer et al. (2010) investigated the outflow from the Labrador Sea based on measurements conducted between 1997 and 2009. They describe intra- to inter-annual variability, but no detectable decadal trend of weakening or strengthening of the deep Labrador Sea outflow has been measured (Fischer et al. 2010).

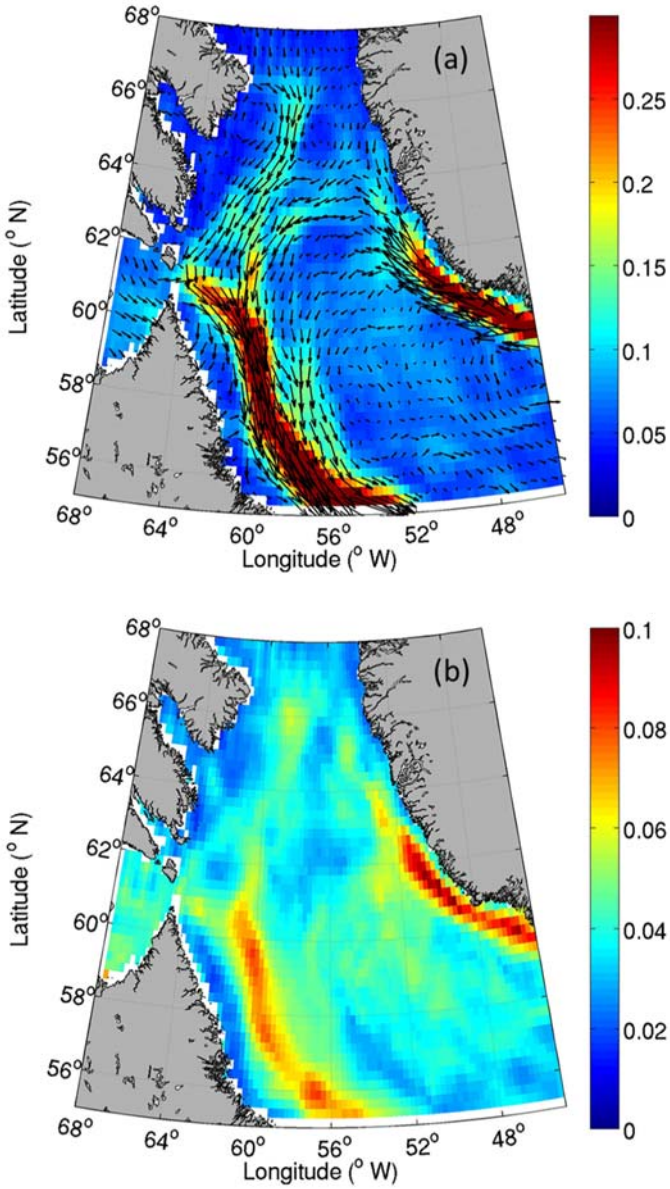

Figure 4.30: Mean surface currents (m s^{-1}) based on monthly AVISO geostrophic currents from 2000 to 2018 in the Davis Strait and northern Labrador Sea. (a) Current speed (m s^{-1}, colours) and direction (vectors), (b) standard deviation (m s^{-1}).

4.3.4 Discussion

The Davis Strait case study area and associated current systems is a key region for the export of Arctic waters into the subpolar Northwest Atlantic. In addition, species rich Geodia sponge assemblages are distributed at depths 200 – 1800 m aligned along the shelf break and continental slope between southern Baffin Island and Newfoundland (Knudby et al. 2013). The water circulation south of Davis Strait is dominated by export of cold and low saline Arctic waters through the Davis Strait and warmer and higher salinity waters from West Greenland retroflection. Those two currents

contribute to form the southward flowing Labrador Current south of 60°N along the Canadian shelf break and slope. In summer 2018, an ATLAS cruise led by DFO Canada on board CCGS Amundsen was conducted to collect new data on physical and biogeochemical water mass properties along two transects inside and outside sponge areas, respectively. Another field experiment to collect additional data in the same area is planned for July 2019. The main aim of the field experiments is to compare and quantify hydrodynamic conditions and water mass properties in sponge and no-sponge areas of the Davis Strait case study area.

5 Summary and concluding remarks

Hydrodynamic controls and mechanisms of organic matter supply to three ATLAS case study areas, i.e. Rockall Bank, Condor Seamount, and Davis Strait, are highlighted in this report. While the Rockall Bank forms the most complete data set of the three study sites, observations from Condor Seamount and Davis Strait are still being progressed. From all study areas available in-situ data are compared to modelled observations. Basin-scale VIKING20 model data (Davis Strait, Rockall Bank, Condor Seamount) and high-resolution local area ROMS model data (Rockall Bank, Condor Seamount) was used for estimating physical drivers of variability patterns in often tidally dominated systems. At the Rockall Bank, in-situ hydrodynamic measurements are in good agreement with the main variability patterns of modelled currents. However, it remains difficult to reproduce exact magnitudes in the models due to comparison of different time periods and intervals of in-situ measurements. At Condor Seamount, modelled currents agree well with published data of mean currents from this area (Bashmachnikov et al. 2013). A high-resolution model for the Davis Strait has not been developed due to the large size of the case study area and limited computational resources. Thus, analysis of model data for the Davis Strait area was mainly based on output from the basin-wide VIKING20 model.

In a recent overview of the Arctic and North Atlantic oceanography, Yashayaev et al (2015) highlighted the importance of developing a better understanding of the AMOC dynamics and its basin-wide variability as a vital prerequisite for more accurate predictions of future climate change. Robust knowledge about characteristic scales and drivers of climate change will also provide the tools for future projections of the effect of a changing ocean climate on deep-sea ecosystems (Sweetman et al 2017). The response of near-bottom and depth-averaged currents to characteristic changes in the basin-wide AMOC based on VIKIN20 model data was visible in all three case study areas. However, characteristic anomalies in the Rockall Bank and Condor Seamount areas were much smaller when compared to changes in the Davis Strait case study area (Figure 2.4 – 2.6). The large carbonate mounds at the south-eastern Rockall Bank and Condor Seamount are areas of intense tide-topography interaction, which generates an energetic dynamical response consisting of a large spectrum of higher frequency motions including freely propagating and trapped internal waves and turbulent mixing (e.g. Bashmachnikov et al. 2013, Cyr et al. 2016).

There are two prinicipal hypotheses of organic matter supply to the deep-sea ecosystems in the Rockall Bank case study area. One hypothesis describes the interaction of tidal currents with the mound structures itself causing a downward transport of organic matter (Soetaert et al. 2016), while the other hypothesis suggests that organic-rich material is transported from shallower regions of the

bank towards the mound structures by cross-slope advection (Duineveld et al. 2007). Particle fluxes and physical oceanographic in-situ measurements at Rockall Bank reveal evidences for both hypotheses but show that there are seasonal differences. These differences might go along with the seasonal influence of different water masses present in the study area. At Condor Seamount, measurements by Bashmachnikov et al (2013) and ATLAS model results identified energetic internal tides and associated local mixing, which may support an important and efficient food supply mechanism for filter feeders atop the Condor summit and along the upper seamount flanks. The episodic formation and shedding of a Taylor cap might support trophic enrichment over the seamount by enhanced horizontal fluxes of planktonic material.

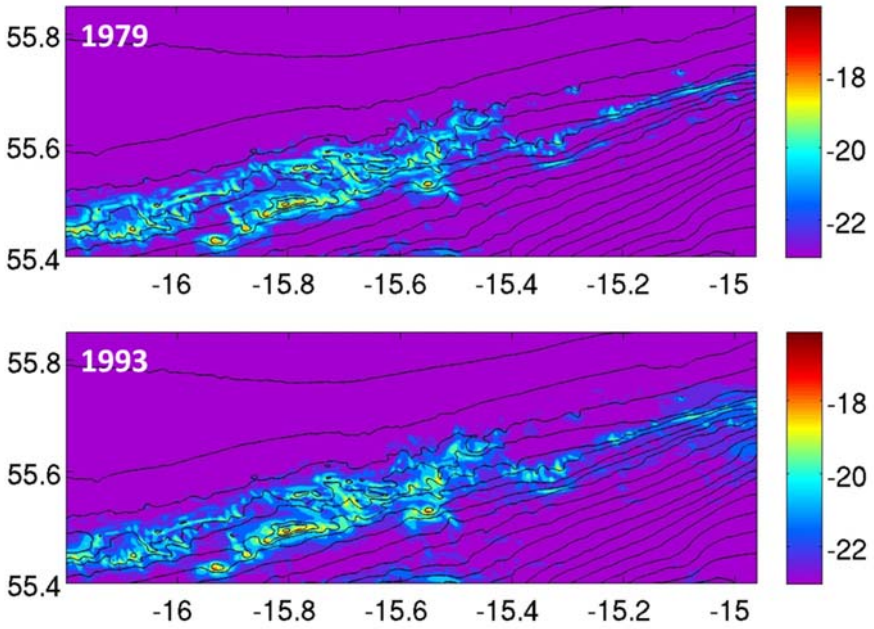

Figure 4.31: Average energy dissipation $\log_{10}$ (Є) [m^2s^{-3}] in the Rockall Bank case study area in 1979 (top) and 1993 (bottom). Energy dissipation was calculated from daily averages of bottom velocities u and v according to $Є = \mu * \rho^{-1} ((\partial u/\partial x)^2 + (\partial v/\partial y)^2)$, μ = dynamic viscosity, ρ = water density. X-axis: Longitude, Y-axis: Latitude. Results are based on high-resolution ROMS simulations.

The large Rockall Bank coral mounds and Condor Seamount are areas of locally enhanced energy dissipation (see Figure 4.31 and 4.32) and areas of potentially increased sediment resuspension through intense turbulent mixing. High-energy dissipation rates in areas of intense flow-topography interaction indicate energy transfer from lower frequency motions towards higher frequencies, e.g. internal waves and turbulent mixing. Thus, energy dissipation provides a dynamical link to benthic ecology. Energy dissipation rates calculated in different AMOC years are presented in Figure 4.31 (Rockall Bank) and Figure 4.32 (Condor Seamount). Although apparent differences in energy

dissipation between different AMOC states appear to be small, they can create strong local differences in horizontal and vertical scales of turbulent mixing. Further data evaluation will be performed to complete the overview of all three study areas.

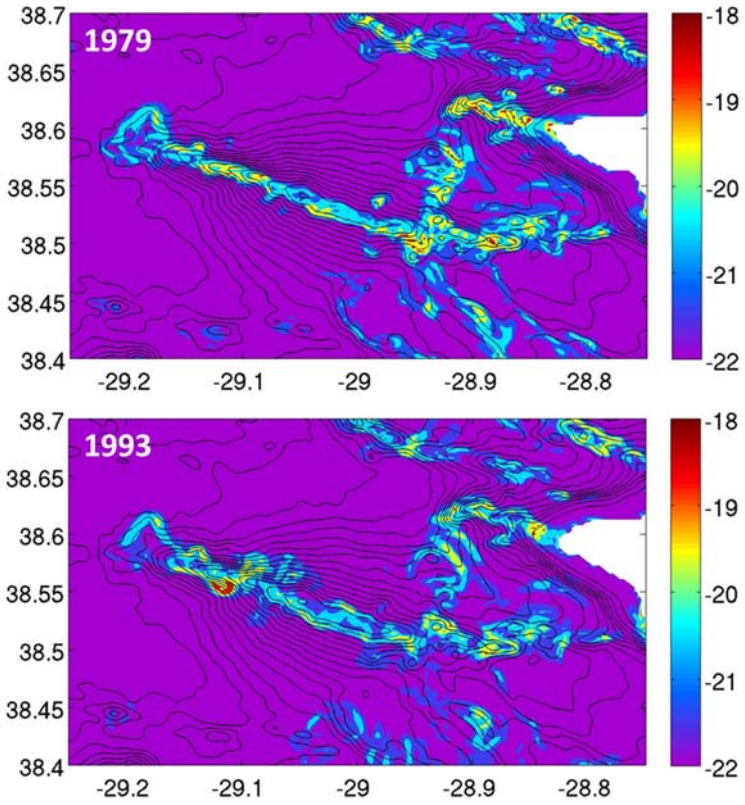

Figure 4.32: Average energy dissipation $\log_{10}$ (Є) [m^2s^{-3}] in the Condor seamount case study area in 1979 (top) and 1993 (bottom). Energy dissipation was calculated from daily averages of bottom velocities u and v according to $Є = \mu * \rho^{-1} * ((\partial u/\partial x)^2 + (\partial v/\partial y)^2)$, μ = dynamic viscosity, ρ = water density. X-axis: Longitude, Y-axis: Latitude. Results are based on high-resolution ROMS simulations.

6 References

Alves, M., Gaillard, F., Sparrow, M., Knoll, M., Giraud, S. (2002) Circulation patterns and transport of the Azores Front–Current system. Deep-Sea Research II 49, 3983–4002. doi:10.1016/S0967-0645(02)00138-8.

Bashmachnikov, I., Mohn, C., Pelegrí, J.L., Martins, A., Jose, F., Machín, F., White, M. (2009) Interaction of Mediterranean water eddies with Sedlo and Seine Seamounts, Subtropical Northeast Atlantic. Deep-Sea Research II 56, 2593–2605. doi:10.1016/j.dsr2.2008.12.036.

Bashmachnikov, I.,Loureiro, C.M., Martins, A. (2013) Topographically induced circulation patterns and mixing over Condor seamount. Deep-Sea Research II 98, 38–51.

Böning, C. W., Behrens, E., Biastoch, A., Getzlaff, K., Bamber, J. L. (2016). Emerging impact of Greenland meltwater on deepwater formation in the North Atlantic Ocean. Nature Geoscience, 9 (7). pp. 523-527. DOI 10.1038/ngeo2740.

Böning, C., Scheinert, M., Dengg, J., Biastoch, A., and Funk, A. (2006) Decadal variability of subpolar gyre transport and its reverberation in the North Atlantic overturning. Geophysical Research Letters, 33, L21S01, doi:10.1029/2006GL026906.

Braga-Henriques, A., Porteiro, F. M., Ribeiro, P. A., de Matos, V., Sampaio, I., Ocana, O., Santos, R.S. (2013). Diversity, distribution and spatial structure of the cold-water coral fauna of the Azores (NE Atlantic). Biogeosciences 10, 4009-4036. https://doi.org/10.5194/bg-10-4009-2013

Cascão, I., Domokos, R., Lammers, M.O., Marques, V., Domínguez, R., Santos, R.S., Silva, M.A. (2017) Persistent Enhancement of Micronekton Backscatter at the Summits of Seamounts in the Azores. Frontiers in Marine Science 4:25. doi: 10.3389/fmars.2017.00025.

Curry, B., Lee, C.M., Petrie, B., Moritz, R.E., Kwok, R. (2014) Multiyear volume, liquid freshwater, and sea Ice transports through Davis Strait, 2004–10. Journal of Physical Oceanography 44, 1244 – 1266.

Cyr, F., Van Haren, H., Mienis, F., Duineveld, G.C.A., Bourgault, D. (2016) On the Influence of Cold-Water Coral Mound Size on Flow Hydrodynamics, and Vice Versa. Geophysical Research Letters 43 (2): 775–783.

Dengler, M., Fischer, J., Schott, F. A., Zantopp R. (2006) Deep Labrador Current and its variability in 1996–2005, Geophysical Research Letters 33, L21S06, doi:10.1029/2006GL026702.

Duineveld, G.C.A., Lavaleye, M.S.S., Bergman, M.I.N, De Stigter, H., Mienis, F. (2007) Trophic structure of a cold-water coral mound community (Rockall Bank, NE Atlantic) in relation to the near-bottom particle supply and current regime. Bulletin of Marine Science 81:449-467.

Egbert, G. D., Erofeeva, S.Y. (2002) Efficient inverse modeling of barotropic ocean tides. Journal of Atmospheric and Oceanic Technology 19-2, 183-204.

Findlay, H. S., et al. (2013) Tidal downwelling and implications for the carbon biogeochemistry of cold-water corals in relation to future ocean acidification and warming. Global Change Biology 19(9), 2708-2719.

Fischer, J., Visbeck, M., Zantopp, R., Nunes, N. (2010) Interannual to decadal variability of outflow from the Labrador Sea. Geophysical Research Letters 37, L24610.

Genin, A. (2004) Bio-physical coupling in the formation of zooplankton and fish aggregations over abrupt topographies. Journal of Marine Systems 50, 3–20.

Genin, A., Dower, J.F. (2007) Seamount plankton dynamics. Seamounts: ecology, fisheries and conservation (ed. by T.J. Pitcher, T. Morato, P.J.B. Hart, M.R. Clark, N. Haggan and R.S. Santos), pp. 85–100. Blackwell Publishing, Oxford.

Giacomello, E., Menezes, G. (Eds.) (2011) CONDOR Observatory for long-term study and monitoring of Azorean seamount ecosystems. Final Project Report. Arquivos do DOP, Série Estudos 1/2012. 261 pp + 9 annexes.

Hatun, H., Sandø, H.B., Drange, H., Hansen, B., Valdimarsson, H (2005). Influence of the Atlantic Subpolar Gyre on the Thermohaline Circulation. Science 309, 1841 - 1844.

Jia, Y (2000) Formation of an Azores Current due to Mediterranean overflow in a modeling study of the North Atlantic. Journal of Physical Oceanography 30, 2342–2358.

Johnson, C., Sherwin, T. D., Smythe-Wright, T. Shimmield, W., Turrell (2010) Wyville Thomson Ridge overflow water: spatial and temporal distribution in the Rockall Trough, Deep Sea Research Part I: Oceanographic Research Papers 57, 1153–1162.

Johnson C., Sherwin T., Cunningham S., Dumont E., Houpert L., Holliday, N. P. (2017) Transports and pathways of overflow water in the Rockall Trough, Deep Sea Research Part I: Oceanographic Research Papers 122: 48– 59.

Kenchington, E., Lirette, C., Cogswell, A., Archambault, D., Archambault, P., Benoit, H., et al. (2010) Delineating Coral and Sponge Concentrations in the Biogeographic Regions of the East Coast of

Canada Using Spatial Analyses. DFO Canadian Scientific Advisory Secretariat Research Document 2010/041.iv, 207 pages.

Klein, B, Siedler, G (1989) On the origin of the Azores Current. Journal of Geophysical Research Oceans 94, 6159–6168. doi:10.1029/JC094iC05p06159.

Knudby, A., Kenchington, E., Murillo, F.J. (2013). Modeling the Distribution of Geodia Sponges and Sponge Grounds in the Northwest Atlantic. PLoS ONE 8(12): e82306. https://doi.org/10.1371/journal.pone.0082306.

Lavelle, J.W., Mohn, C. (2010) Motion, commotion, and biophysical connections at deep ocean seamounts. Oceanography 23 (1), 90 - 103.

Lozier, M.S., Owens, W.B., Curry, R.G. (1995) The climatology of the North Atlantic. Progress in Oceanography 36, 1–44. doi:10.1016/0079-6611 (95)00013-5.

Mason, E., Coombs, S., Oliveira, P.B. (2006). An overview of the literature concerning the Oceanography of the eastern North Atlantic region. Relat. Cient. Tec. IPIMAR, Série digital, (http://ipimar-iniap.ipimar.pt) 33, 58 pp.

McGrath, T., Nolan G., McGovern, E. (2012) Chemical characteristics of water masses in the Rockall Trough. Deep Sea Research Part I: Oceanographic Research Papers, Vol 61, pp 57-73

Mienis, F., Van Weering, T., De Haas, H., De Stigter, H., Huvenne, V., Wheeler., A. (2006) Carbonate Mound Development at the SW Rockall Trough Margin Based on High Resolution TOBI and Seismic Recording. Marine Geology 233 (1–4), 1–19.

Mohn, C., Rengstorf, A., White, M., Duineveld, G.C.A., Mienis, F., Soetaert, K., Grehan, A. (2014) Linking Benthic Hydrodynamics and Cold-Water Coral Occurrences: A High-Resolution Model Study at Three Cold-Water Coral Provinces in the NE Atlantic. Progress in Oceanography 122: 92–104.

Murillo, F.J., Muñoz, P.D., Cristobo, J., Ríos, P., González, C., Kenchington, E., Serrano, A. (2012) Deep-sea sponge grounds of the Flemish Cap, Flemish Pass and the Grand Banks of Newfoundland (Northwest Atlantic Ocean): Distribution and species composition. Marine Biology Research 8:9, 842-854, DOI:10.1080/17451000.2012.682583

New, A.L., Jia, Y., Coulibaly, M., Dengg, J. (2001) On the role of the Azores Current in the ventilation of the North Atlantic Ocean. Progress in Oceanography 48, 163-194.

Palma, C., Lillebø, A.I., Borges, C., Souto, M., Pereira, E., Duarte, A.C., Pinto de Abreu, M. (2012) Water column characterisation on the Azores platform and at the sea mounts south of the archipelago, Marine Pollution Bulletin 64 (9), 1884-1894.

Pingree, R.D. (1997) The eastern subtropical gyre (North Atlantic): Flow rings recirculations structure and subduction. Journal of the Marine Biological Association of the United Kingdom, 77, 573-624.

Richardson, P.L., Bower, A., Zenk, W. (2000) A census of Meddies tracked by floats. Progress Oceanography 45, 209–250. doi:10.1016/S0079-6611 (99)00053-1

Ríos, A.F., Pérez, F., Fraga, F. (1992) Water masses in the upper and middle North Atlantic Ocean east of the Azores. Deep-Sea Research 3 - 4, 645-658.

Roberts, J. M., et al. (2006) Reefs of the Deep: The Biology and Geology of Cold-Water Coral Ecosystems. Science 312(5773): 543-547.

Sangrà, P., Pascual, A., Rodríguez-Santana, A., Machín, F., Mason, E., McWilliams, J.C., Pelegrí, J.P., Dong, C., Rubio, A., Arístegui, J., Marrero-Diaz, A., Hernandez-Guerra, A., Martínez-Marrero, A., Auladell, M. (2009) The Canary Eddy Corridor: a major pathway for long-lived eddies in the subtropical North Atlantic. Deep-Sea Research I 56, 2100–2114. doi:10.1016/j.dsr.2009.08.008

Santos, M., Moita, M.T.,Bashmachnikov, I., Menezes, G.M., Carmo, V., Loureiro, C.M., Mendonça, A., Silva, A.F., Martins, A. (2013) Phytoplankton variability and oceanographic conditions at Condor seamount, Azores (NE Atlantic). Deep-Sea Research II 98, 52-62.

Shapiro, G.I., Meschanov, S.L., Emelianov, M.V. (1995) Mediterranean lens “Irving” after its collision with seamounts. Oceanologica Acta 18, 309–318.

Shchepetkin, A.F., McWilliams, J.C. (2005) The Regional Ocean Modeling System (ROMS): a split-explicit, free-surface, topography following-coordinate oceanic model.Ocean Modelling 9, 347 - 404.

Soetaert, K., Mohn, C., Rengstorf, A., Grehan, A., van Oevelen, D. (2016) Ecosystem engineering creates a direct nutritional link between 600-m deep cold-water coral mounds and surface productivity. Scientific Reports 6:35057.

Sutherland, D., Pickart, R. (2008) The East Greenland Coastal Current: Structure, variability, and forcing. Progress in Oceanography 78, 58–77, doi:10.1016/j.pocean.2007.09.006.

Straneo, F., Saucier, F. (2008) The outflow from Hudson Strait and its contribution to the Labrador Current. Deep-Sea Research I 55, 926– 946.

Sweetman, A.K., Thurber, A.R., Smith, C.R., Levin, L.A., Mora, C., Wei, C.-L., Gooday, A.J., Jones, D.O. B., Rex, M., Yasuhara, M., Ingels, J., Ruhl, H.A., Frieder, C.A., Danovaro, R., Würzberg, L., Baco, A., Grupe, B.M., Pasulka, A., Meyer, K.S., Dunlop, K.M., Henry, L.-A., Roberts, J.M. (2017) Major impacts of climate change on deep-sea benthic ecosystems. Elementa Science of the Anthropocene, 5: 4, DOI: https://doi.org/10.1525/elementa.203.

Tang, C., Ross, C., Yao, T., Petrie, B., DeTracey, B., Dunlap, E. (2004) The circulation, water masses and sea-ice of Baffin Bay. Progress in Oceanography, 63, 183–228.

Tempera, F., Giacomello, E., Mitchell, N.C., Campos, A.S., Braga Henriques, A., Bashmachnikov, I., Martins, A., Mendonça, A., Morato, T., Colaço, A., Porteiro, F.M., Catarino, D., Gonçalves, J., Pinho, M.R., Isidro, E.J., Santos, R.S., Menezes, G. (2012) 59 - Mapping Condor Seamount Seafloor Environment and Associated Biological Assemblages (Azores, NE Atlantic), Editor(s): Peter T. Harris, Elaine K. Baker, in: Seafloor Geomorphology as Benthic Habitat, Elsevier, 807-818. ISBN 9780123851406, https://doi.org/10.1016/B978-0-12-385140-6.00059-1.

Van Bleijswijk, J.D.L., Whalen, C., Duineveld, G.C.A., Lavaleye, M.S.S., Witte, H.J., Mienis, F. (2015) Microbial Assemblages on a Cold-Water Coral Mound at the SE Rockall Bank (NE Atlantic): Interactions with Hydrography and Topography. Biogeosciences 12 (14): 4483–4496.

Van Haren, H., Mienis, F., Duineveld, G.C.A., Lavaleye, M.S.S. (2014) High-Resolution Temperature Observations of a Trapped Nonlinear Diurnal Tide Influencing Cold-Water Corals on the Logachev Mounds. Progress in Oceanography 125: 16–25.

Van Soest, R.W.M., Lavaleye, M.S.S. (2005) Diversity and Abundance of Sponges in Bathyal Coral Reefs of Rockall Bank, NE Atlantic, from Boxcore Samples Published in Collaboration with the University of Bergen and the Institute of Marine Research, Norway, and the Marine Biological Laboratory, Unive. Marine Biology Research 1 (5): 338–349.

Van Weering, T. C.E., De Haas H., De Stigter H.C., Lykke-Andersen H., Kouvaev I. (2003) Structure and Development of Giant Carbonate Mounds at the SW and SE Rockall Trough Margins, NE Atlantic Ocean. Marine Geology 198 (1–2): 67–81.

Wang, G., Dewar, W.K. (2003) Meddy–Seamount interactions: implications for the Mediterranean salt tongue. Journal of Physical Oceanography 33, 2446–2461.

White, M., Roberts, J.M., van Weering, T. (2007). Dp bottom-intensified diurnal tidal currents shape the alignment of carbonate mounds in the NE Atlantic? Geo-Marine Letters 27: 391 - 397.

Wilson, C.D., Boehlert, G.W. (2004). Interaction of ocean currents and resident micronekton at a seamount in the central North Pacific. Journal of Marine Systems 50, 39–60.

Wu, Y., Hannah, C.G., Petrie, B., Pettipas, R., Peterson, I., Prinsenberg, S., Lee, C.M., Moritz, R. (2013) Ocean current and sea ice statistics for Davis Strait. Canadian Technical Report of Hydrography and Ocean Sciences 284: vi, 47p.

Yashayaev, I., Seidov, D., Demirov, E. (2015) A new collective view of oceanography of the Arctic and North Atlantic basins. Progress in Oceanography 132, 1 - 21.

Document Information

EU Project N°	678760	**Acronym**	ATLAS
Full Title	A trans-Atlantic assessment and deep-water ecosystem-based spatial management plan for Europe		
Project website	www.eu-atlas.org		

Deliverable	**N°**	2.4	**Title**	Water mass properties, hydrodynamic controls and mechanisms of organic matter supply in ATLAS case study areas
Work Package	**N°**	2	**Title**	Functional Ecosystems

Date of delivery	**Contractual**		**Actual**	
Dissemination level	PU	PU Public, fully open, e.g. web		
		CO Confidential restricted under conditions set out in Model Grant Agreement		
		CI Classified, information as referred to in Commission Decision 2001/844/EC		

Authors (Partner)	AU, NIOZ			
Responsible Authors	**Name**	Christian Mohn	**Email**	chmo@bios.au.dk
		Dick van Oevelen		Dick.van.Oevelen@nioz.nl

Version log			
Issue Date	**Revision N°**	**Author**	**Change**